MÁSTER UCM EN ASTROFÍSICA


UNIVERSIDAD COMPLUTENSE
MADRID

# Star-Forming Galaxies at z~0.61

Trabajo Fin de Máster

Carlos Gómez Guijarro

Septiembre 2014

Trabajo dirigido por Dr. Jesús Gallego Maestro

Tutor UCM: Dr. Jesús Gallego Maestro

DEPARTAMENTO DE ASTROFÍSICA Y CIENCIAS DE LA ATMÓSFERA

# Contents

# 1. Introduction

The study of the galaxy population of the Universe requires a series of observables to compare the different physical properties along its history. One of these observables is the star formation rate density (SFRd). This magnitude traces the average star formation rate (SFR), in other words, the gaseous mass that is transformed into stars per unit volume and time.

The star formation rate density has been a topic of study in the last decades. Since the first work (Madau et al., 1996) to the present day different results have been obtained up to $z \sim 10$ employing several tracers from X-rays to radio emission (Hopkins & Beacom, 2006). The cosmic SFRd grows from the origin of the first galaxies and peaks at $z \sim 2$-3 (Madau & Dickinson, 2014). It becomes constant up to z=1 and then falls down 10-20 times to z=0 (Gallego et al., 1995).

In order to measure the cosmic star formation history it is needed to build samples of star-forming galaxies (SFGs). Several techniques have been developed to identify them. In this work we make use of a narrow-band filter to select the SFGs by their emission lines. This method has several advantages. It permits very deep surveys in a narrow region in terms of redshift, selecting the candidates directly from the emission line we want to study. In addition, these filters are more effective in the detection of weak sources. On the other hand, there are disadvantages such as dust obscuration, AGN contamination and insensibility to low equivalent widths.

The deep near-infrared (NIR) surveys are crucial to test galaxies evolution form intermediate to high redshifts. Tracing rest-frame optical it is possible to calculate several parameters as the galaxy mass. Moreover, there are several emission lines in the optical that are indicative of star formation. One of them is $H\alpha$ (Kennicutt, 1998), that we employ in this work.

Star-forming regions are surrounded by clouds of gas and dust. The most massive and young stars emit Lyman photons, ionizing the gas, mainly composed of hydrogen atoms. When recombination occurs hydrogen line series appear and $H\alpha$ $\lambda 6562.8\,\text{Å}$ is one of the strongest emission lines in the optical. The stars that produce an ionizing flux are very young, with ages below 20 Myr and masses above $10\ M_\odot$. We say that $H\alpha$ is a tracer of the instantaneous SFR. It has the advantage of a direct relation between the number of young stars and the line intensity. Furthermore, the dependence on the metallicity of the gas is negligible. However, $H\alpha$ has some drawbacks, like high dependence on the initial mass function, not being sensitive to masses below $10\ M_\odot$. It is also an indicator affected by obscuration, but much less than other tracers like ultraviolet (UV). The different tracers of the star formation history provide a comprehensive and consistent view of the evolution of star formation. However, there are discrepances between the results obtained with different indicators at the same redshift. This is due to selection methods, extinction dependence or sensitivity to a different stellar mass. $H\alpha$, being a direct tracer of the instantaneous star formation in a galaxy (Kennicutt & Evans, 2012), is a good candidate for a precise study of the SFRd evolution with redshift.

In this work we present a sample of 41 SFGs at $z \sim 0.61$ selected by their emission in $H\alpha$ line to measure the SFRd at this redshift and to obtain a deep view of the SFGs population at this epoch. We describe the sample selection in Section 2. Section 3 contains the method to get the fluxes, luminosities and extinction. In Section 4 we study the global properties of the sample such as luminosity function (LF), SFRd and spacial distribution. In Section 5

we include an analysis about physical properties of the sample such as extinction and SFR relation and the main sequence of SFGs. In Section 6 we show a morphological classification. Section 7 includes the spectroscopic outcome. We summarize our results and conclusions in Section 8. In addition, we include three appendices: Appendix A contains the tables of the measurements and the derived physical properties of the sample. Galaxy RGB images are included in Appendix B. 1D spectra are shown in Appendix C.

To complement this document and to provide a legacy of this TFM we have developed a webpage of the sample[1]. It is build using HTML code and it is included in the UCM group of Extragalactic Astrophysics and Astronomical Instrumentation (GUAIX) website. The reader should find there all the data concerning each object of the sample, as well as RGB images and spectra, if it is available.

Throughout this work we adopt a cosmology with $[\Omega_\Lambda, \Omega_M, h] = [0.7, 0.3, 0.7]$. Considering these parameters the age of the Universe at z=0.61 is 7.69 Gyr, the luminosity distance is 3601.6 Mpc and the scale 6.736 kpc/arcsec. AB magnitude system is employed over the whole study.

## 2. VLT/HAWK-I survey. The sample selection

The data used in this work correspond to very deep observations of the Great Observatories Origins Deep Survey South (GOODS-S) field with the High Acuity Wide field K-band Imager (HAWK-I) of the Very Large Telescope (VLT) UT4 8.2 m. The field of view of this instrument is 7.5' x 7.5' (Kissler-Patig et al., 2008; Siebenmorgen et al., 2011).

The observations were carried out between September 2008 and April 2010, with a total of 32 hours of integration in the narrow-band filter (project 181.A-0485(A) Clément et al. (2012)). This project was aimed to detect Lyman $\alpha$ emitters (LAEs) at z=7.7 in order to constrain the epoch of reionization. The field was choose for the avaibility of multiwavelength data. These deep images provide secondary observations of $H\alpha$ emitters that we employ in this work.

An observation technique in a narrow-band filter is used to select the candidates. The image in this band is compared with a broad-band one. Those objects with a redshift z $\sim$0.61 and intense $H\alpha$ emission line present a flux excess in the narrow-band filter, centered on the line, compared to the broad-band used to measure the continuum. In this study the $H\alpha$ line moves into NIR, specifically into the J-band.

The broad-band filter employed is the J-band, while the narrow-band is the NB1060. For z=0.61 the $H\alpha$ line, located at $\lambda$6562.8 Å in rest-frame ($\lambda_0$), shifts to $\lambda$10619 Å ($\lambda_z$). The relation between both wavelenghts through redshift is $\lambda_z = \lambda_0(1+z)$. The effective width of the narrow-band filter is 108Å. We are going to use this value later in order to determine the minimum and maximum redshifts for which we can detect the objects.

The selection process of the galaxy sample is performed through a color-magnitude diagram (Pascual et al., 2007). The (broadband - narrowband) color is represented as a function of the narrowband magnitude. The objects that present emission line will give us a flux excess in the narrowband and will move to higher positions in the diagram. A selection criteria more

[1] http://guaix.fis.ucm.es/node/1586

restrictive as we move to fainter magnitudes is employed. The galaxies above this criterion are selected as emission-line objects and we identify themo as galaxies with intense star formation. The limit in terms of the equivalent width is $EW(H\alpha) > 10\,\text{Å}$. Once this procedure is carried out, we get a total sample of 46 galaxies.

The data reduction and astrometic calibration was performed by J.G.Cuby team at the Observatoire de Marseille. Víctor Villar and Jesús Gallego conducted the selection of the candidates. This project complements previous studies carried out by the UCM group using $H\alpha$ at different redshifts (Gallego et al., 1995; Pascual et al., 2001; Pascual, 2005; Villar et al., 2008).

## 2.1. The CANDELS Survey

The Cosmic Assembly Near-IR Deep Extragalactic Legacy Survey (CANDELS) (Grogin et al., 2011; Koekemoer et al., 2011) is a powerful imaging survey of the distant Universe being carried out with the *Hubble Space Telescope* (*HST*). It is the largest project of *HST* to date. It is designed to study the galactic evolution from z=8 to 1.5. To accomplish this objective it employs deep imaging of more than 250,000 galaxies with WFC3/IR and ACS instruments.

For the present work, we are interested in the advanced data products that CANDELS project has recently released in the GOODS-S field. CANDELS GOODS-S Multiwavelenght catalog (Guo et al., 2013) presents the multiwavelenght photometry available in this field. It combines the newly obtained data from HST/WFC3 F105W, F125W and F160W with public data. This catalog is based on source detection in the WFC3 F160W mosaic, that includes the data from CANDELS deep and wide programs. The result is a catalog of 34,930 sources in an area of 173 square arcmin. Apart from the WFC3 bands, this catalog includes UV data (U band form CTIO/MOSAIC and VLT/VIMOS), optical (HST/ACS F435W, F606W, F775W, F814W and F850LP) and IR (*HST*/WFC3 F098M, VLT/ISAAC Ks, VLT/HAWK-I Ks, and Spitzer/IRAC 3.6, 4.5, 5.8, 8.0 $\mu$m).

This catalog is employed in this work to collect several measurements required for our study. Equatorial coordinates, photometric redshifts, masses, sizes, synthetic data such as IR luminosity and UV magnitudes and a variety of photometric measurements are taken from this catalog.

We do several verifications through the CANDELS data. First of all, we check the original sample, founding counterparts for 42 galaxies of the 46 original sample. Searching for the 4 missing candidates in the CANDELS Display we find that HAWKI0003148 and HAWKI0003151 leave the display field. HAWKI0003361 is a star or it is affected by the emission of a close one. Lastly, in the region of the candidate HAWKI0003606 there are no signals of an object.

Secondly, we confirm the preliminary determination of the photometric redshifts from *Rainbow* database (Barro et al., 2011) and replace them with the CANDELS ones, more precisely calculated. In order to verify CANDELS photometric redshifts, we cross-check them with the available spectroscopic data (Figure 1). The majority of the objects (11/13) show the same result within uncertainties. Therefore, approximately, in a 85%(11/13) of the cases the photo-z are well determined. Apart from this, we can estimate how many of our objects are real $H\alpha$ emitters. A 93.5%(12/13) are object spectroscopically confirmed as emitters of a line at

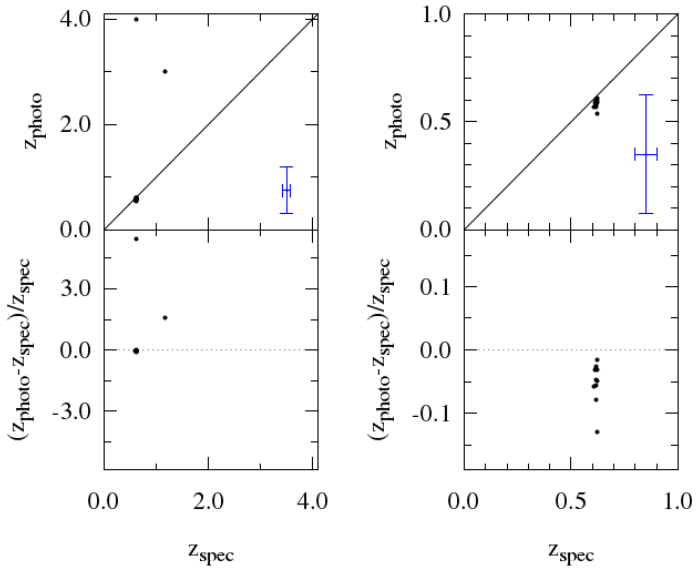


Figure 1: photo-z taken from CANDELS survey vs spec-z taken from ancillary data. Left: in the upper plot an scatter of the points with the 1:1 relation; in the lower plot the dispersion of photo-z in terms of spec-z. Right: a zoom of the $0 < z < 1$ region of the left panel. In blue it is shown the average error.

z$\sim$0.61. We can conclude that a 93.5% of the sample are real $H\alpha$ emitters.

## 2.2. Spectroscopic sample

In order to complete the information of the sample, we carry out a search of the spectroscopic data available in existing published studies. In the first place, we perform a complete search in the European Southern Observatory (ESO), Centre de Données astronomiques de Strasbourg (CDS) and The VIMOS VLT Deep Survey (VVDS) archives, as well as throughout the literature in the GOODS-S field. We find a total of 13 spectroscopic redshifts, which we have used in the previous section to test the photometric ones. Among them, 8 FITS full spectrum for 7 different galaxies are found (Le Fèvre et al., 2004; Vanzella et al., 2008; Balestra et al., 2010). The rest of the objects with no spectra available correspond to Guo et al. (2013), where they refer to Dahlen et al. (2010). We do not find new results in the last reference and in the fifteen named there, where the authors find their spec-z. Finally, we contact with the University of California to request for any Keck spectroscopy thanks to the collaboration that the director of this work keeps with them. However, the answer was negative, no spectra are publically accessible for these objects. In the Appendix B it is included all the spectra obtained for the sample.

Once the original sample is checked, we discard four candidates (HAWKI0003148, HAWKI0003151, HAWKI0003361 and HAWKI0003606) with no counterparts in the CANDELS Survey and one more (CANDELS 16483) due to a spectroscopically confirmation of an emission line different from $H\alpha$. Therefore, the final sample for this project is composed of 41 galaxies with $H\alpha + [NII]$ emission. We refer the following calculations and results to it unless otherwise stated.

# 3. Fluxes, luminosities and extinction

## 3.1. Line flux

Line and continuum fluxes are the basic measurements from which we carry out the calculations. In this section we are going to explain how these fluxes are obtained. We follow here the Pascual et al. (2007) approach.

The combination of a narrow-band filter and a broad-band filter allows us to determine the line flux ( $f_l$ ) and the continuum flux ( $f_\lambda^C$ ). We assume that the effective width of the broad-band is much larger than the narrow-band ( $\Delta_{BB}^{'} \gg \Delta_{NB}^{'}$ ). In addition, we consider that the continuum flux is nearly constant.

$$f_l = \Delta_{NB}^{'}(\bar{f}_\lambda^{NB} - \bar{f}_\lambda^{BB}) \tag{1}$$

$$f_\lambda^C = \bar{f}_\lambda^{BB} \tag{2}$$

The $\lambda$ subscript indicates flux densities and $\bar{f}_\lambda^{NB}$ y $\bar{f}_\lambda^{BB}$ are the mean fluxes in the narrow-band and broad-band filters.

However, there is a problem in determining the $H\alpha$ line flux. This line is flanked by $[NII]\lambda 6548, 6584\,\text{Å}$. To get rid of this effect it is applied the following expression:

$$\bar{f} = \bar{f}_C + \left( \frac{1}{\Delta'(\lambda_z^1)} + \frac{1}{\Delta'(\lambda_z^2)} \frac{f_l^2}{f_l^1} + \frac{1}{\Delta'(\lambda_z^3)} \frac{f_l^3}{f_l^1} \right) f_l^1 \tag{3}$$

where $f_l^1$ , $f_l^2$ and $f_l^3$ are the line fluxes and $\lambda_z^1$ , $\lambda_z^2$ and $\lambda_z^3$ are their redshifted wavelengths.

Thus, it is possible to calculate the line flux of a single line knowing the ratio with the other two. For more information about this process see Pascual et al. (2007).

In Figure 2 a histogram of the line fluxes is shown. Typical uncertainties are $1 \times 10^{-18}$erg s$^{-1}$cm$^{-2}$ .

## 3.2. Emission-line luminosity

We calculate the line luminosity via the line flux with the following equation:

$$L = 4\pi d_l^2(z) f_l \tag{4}$$

We also need to know the redshift ( $z$ ) of the objects to obtain the luminosity distance ( $d_l(z)$ ). We employ the spectroscopic values if available. For those objects with no spectroscopic information we take the average redshift z=0.61. The luminosity distance is determined using the cosmologial library *Milia* (Pascual et al., 2007), written in C++. It is accesible in the GUAIX website. This library uses elliptic functions for the computation of the distance (Kantowski et al., 2000).

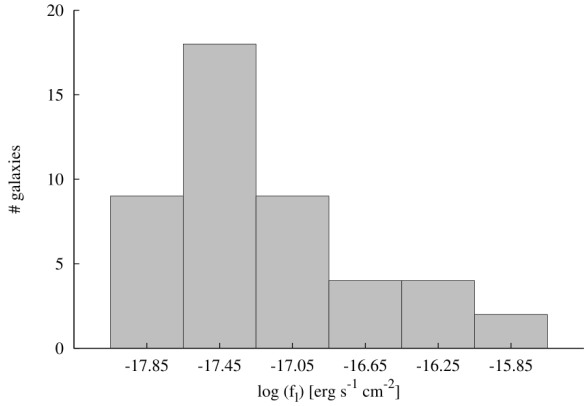


Figure 2: Histogram of the $H\alpha$ line fluxes. We see there is a high number of galaxies as the emission is weaker, but once the detection limit is reached the number decrease drastically. In this case we include the 46 candidates of the original raw sample.

### 3.3. Extinction

So far, we have referred to the flux and luminosity as observed values, hence uncorrected from extinction. Nevertheless, we need to develop a strategy to take into account the various sources of attenuation: the intrinsic extinction from the studied galaxy and the extinction from our own Galaxy. The next expressions show the corrected flux and luminosity:

$$\log f_{l,cor} = \log f_l + 0.4\,(A_{\lambda_0} + a_{\lambda_z}) \tag{5}$$

$$L = 4\pi d_l^2(z) f_{l,cor} \tag{6}$$

where $A_{\lambda_0}$ is the intrinsic extinction of the studied galaxy at rest-frame wavelenght. $a_{\lambda_z}$ is the Galactic attenuation at the observed frame field.

For $a_{\lambda_z}$ we take a constant value of 0.006 mag. It is measured in UKIRT J-band (1.25 $\mu m$) for the coordinates of GOODS-S field (Schlafly & Finkbeiner, 2011). It is a completely negligible value compared with the intrinsic extinction.

Moreover, it is known that the dust absorbs an amount of the star emission. This dust emits it again in the IR. Therefore, a good approach to calculate dust absortion is to study the ratio between dust and far ultraviolet (FUV) fluxes ( $F_{dust}/F_{FUV}$ ). This value is related with the FUV extinction $A_{FUV}$ (Buat et al., 2005):

$$A_{FUV} = -0.0333y^3 + 0.3522y^2 + 1.1960y + 0.4967 \tag{7}$$

$$y = \log\left(\frac{F_{dust}}{F_{FUV}}\right)$$

For those galaxies with IR data measured using MIPS instrument in 24 $\mu$m it is calculated the total infrared luminosity ( $L_{TIR}$ ). On the other hand, the FUV flux is determined synthetically by fitting the filter profile with the Spectral Energy Distribution (SED).

Then, we can obtain the $H\alpha$ extinction ( $A_{H\alpha}$ ) with the $A_{FUV}$ value applying a Calzetti extinction law (Calzetti et al., 2000):

$$A_{H\alpha} = A_{FUV}\frac{k_{H\alpha}}{k_{FUV}} \tag{8}$$

$$k_{H\alpha} = 2.659\left(-1.857 + \frac{1.040}{\lambda_{FUV}}\right) + R'_V$$

$$k_{FUV} = 2.659\left(-2.156 + \frac{1.509}{\lambda_{H\alpha}} - \frac{0.198}{\lambda^2_{H\alpha}} + \frac{0.011}{\lambda^3_{H\alpha}}\right) + R'_V$$

$$R'_V = 4.05$$

However, there are two objects with no available data in MIPS 24 $\mu$m. So, in these cases, we employ FUV (far ultraviolet) and NUV (near ultraviolet) synthetic magnitudes. The color $FUV - NUV$ is related with the ratio $F_{dust}/F_{FUV}$ (Muñoz-Mateos et al., 2009):

$$\frac{L_{TIR}}{L_{FUV}} = 10^{0.30+1.15(FUV-NUV)} - 1.64 \tag{9}$$

Once we have the ratio $L_{TIR}/L_{FUV}$ , we can substitute in the $A_{FUV}$ expression and apply a Calzetti law. In Section 5 we provide average values and distribution.

# 4. Sample properties

## 4.1. Luminosity function

In this section we are going to calculate the luminosity function of the sample (LF) for the line $H\alpha$. This LF determines how the SFR is distributed among the galaxy sample. In the first place, we determine the observed LF, and then, the extinction corrected LF.

To build our LF we employ the $V/V_{max}$ method (Schmidt, 1968). The number of galaxies per unit volume and $\Delta \log L$ interval is:

$$\phi(\log L) = \frac{1}{\Delta \log L \cdot \Omega}\sum_i \frac{1}{V^i_{max}} \tag{10}$$

where $V^i_{max}$ is the maximum volume in which we can detect the $i$ object per unit volume and $\Omega$ is the solid angle of the survey.

We need to obtain $V^i_{max}$. We consider that the galaxies can be detected in the redshift interval of the narrow-band filter effective width. This interval is $0.6098 < z < 0.6263$. The maximum volume of detection is the difference between the comoving volume at these redshifts.

To calculate the comoving volume we use once again the *Milia* library, providing us this value per solid angle. As the survey field is 7.5' x 7.5', the solid angle is $\Omega = 4.7597 \times 10^{-6}\,\mathrm{srad}$ . The maximum volume of detection for each galaxy is then $V^i_{max} = 2.5681 \times 10^8\,\mathrm{Mpc}^3/\mathrm{srad}$. Hence, the volume covered by this survey is $1222\,\mathrm{Mpc}^3$. A small volume as a consequence of being a narrow-band survey with a smaller field compared with similar studies (Villar et al. (2008) at z$\sim$0.84 has a 15.4' x 15.4' field).

Making use of the previous values, we can calculate the LF. We fit each result to a Schechter function (Schechter, 1976; Gallego et al., 1995):

$$\phi(L)dL = \phi^* \left(\frac{L}{L^*}\right)^{\alpha} \exp\left(-\frac{L}{L^*}\right) \frac{dL}{L^*} \tag{11}$$

Here, $L^*$ is a characteristic galaxy luminosity where the power-law form of the function cuts off. The parameter $\phi^*$, with units of number density, provides the normalization. $\alpha$ is the faint-end slope of the LF.

### 4.1.1. Observed and extinction corrected luminosity function

In the first place, we obtain the observed luminosity function. We choose a luminosity bin $\Delta \log L = 0.4\,\mathrm{erg\ s^{-1}}$ and a first limit $\log L = 39.6\,\mathrm{erg\ s^{-1}}$. These two values are those that provide an optimal agreement between LF resolution and a sufficient number of galaxies per bin so that the statistics are reliable. To determine the extremes of each LF point, the vertical error bars, we consider the uncertainty in the number of galaxies as Poissonian, so if the number of objects is $N$, the uncertainty is $\sqrt{N}$.

Secondly, we perform an extinction correction of the LF. In similar studies authors use the canonical extinction $A_{H\alpha} = 1\,\mathrm{mag}$ (Geach et al., 2008; Sobral et al., 2012). Other authors argue that this value is understimated as redshift grows (Villar et al., 2008; An et al., 2014) and they use an extinction correction for each object individually. We decide to apply the canonical extinction first and then take a more precise approach with the calculation of the extinction for each object as explained in Section 3.3. In this case, we operate with a bin $\Delta \log L = 0.4\,\mathrm{erg\ s^{-1}}$ and a first limit $\log L = 40.0\,\mathrm{erg\ s^{-1}}$.

Before getting the final results, we fit the LF using several values of the $\alpha$ parameter found through the literature. The most common values are $\alpha = -1.3$ (Gallego et al., 1995), $\alpha = -1.35$ (Geach et al., 2008) and $\alpha = -1.6$ (Sobral et al., 2012). In this work, we find the best fitting results for $\alpha = -1.3$, so we use this value from now on.

Apart form this, the uncertainties are firstly calculated using a typical Lavenberg-Marquardt algorithm, leading to very high values. We perform simulations to get a more correct estimation of the errors. We do 10000 simulations in which we variate each point of the LF in the range of its error bar with a uniform probability. We fit the Schechter function for each case. In the end, we have 10000 values of the LF parameters $L^*$ and $\phi^*$ following a Gaussian distribution. The final uncertainties for these parameters are the standard deviation of its distribution. For this process, we employ the scientific library GNU Scientific Library (GSL) built for C/C++.

In Figure 3 we present the LF and its Schechter fit and in Table 1 we collect the numerical results. As a consequence of the extinction correction the LF moves to the right towards

brighter values. We can see a deep insight in the faint-end of the LF. The survey is extremely deep, with 32 hours of integration time. Consequently, we have flux detection limit $> 1.7 \times 10^{-18}\,\mathrm{erg\ s^{-1}cm^{-2}}$, permitting to get data of a very faint population of galaxies never seen before at this redshift. On the other hand, the characteristic of the survey has some drawbacks. The small field of the instrumentation for this kind of research leads us to detect approximately a quarter of the number of galaxies sampled in similar studies (Villar et al., 2008). The brighter the galaxy the smaller the number of them, so we lack of galaxies at the bright-end of the LF. To show this, we perform a simulation of the galaxies we should see at the bright-end. We take the data from our previous study of the sample (Gómez Guijarro, 2013). $\phi^* = 10^{-2.88}\,\mathrm{Mpc^{-3}}$ and $L^* = 10^{42.87}\,\mathrm{erg\ s^{-1}}$ produce results in agreement with the evolution of the SRFd. The simulation results (Table 2) indicate that it would be possible not to detect galaxies in the bright bins for the volume covered in this project as the number of them in those bins would be $2 \pm 1.4$ and $1 \pm 1$.

Table 1: Observed LF and extinction corrected LF. The columns show the values: (1) $H\alpha$ luminosity in erg $s^{-1}$ (logarithmic scale); (2) density of emitters in $\mathrm{Mpc^{-3}}$ (logarithmic scale); (3) number of emitters

| Observed LF | | | Extinction corrected LF | | |
|---|---|---|---|---|---|
| log L(H$\alpha$) (1) | log $\phi$ (2) | # galaxies (3) | log L(H$\alpha$) (1) | log $\phi$ (2) | # galaxies (3) |
| 39.4 | -1.69 ± 0.17 | 10 ± 3.2 | 39.8 | -1.58 ± 0.14 | 13 ± 3.6 |
| 39.8 | -1.49 ± 0.12 | 16 ± 4 | 40.2 | -1.58 ± 0.14 | 13 ± 3.6 |
| 40.2 | -1.84 ± 0.21 | 7 ± 2.6 | 40.6 | -1.79 ± 0.19 | 8 ± 2.8 |
| 40.6 | -2.21 ± 0.37 | 3 ± 1.7 | 41.0 | -1.99 ± 0.26 | 5 ± 2.2 |
| 41.0 | -2.21 ± 0.37 | 3 ± 1.7 | 41.4 | -2.39 ± 0.53 | 2 ± 1.4 |
| 41.4 | -2.39 ± 0.53 | 2 ± 1.4 | | | |
| $\phi^* = 10^{-2.44\pm0.09}\,\mathrm{Mpc^{-3}}$ $\mathrm{L}^* = 10^{41.41\pm0.17}\,\mathrm{ergs^{-1}}$ $\alpha = -1.3$ | | | $\phi^* = 10^{-2.35\pm0.35}\,\mathrm{Mpc^{-3}}$ $\mathrm{L}^* = 10^{41.5\pm1.1}\,\mathrm{ergs^{-1}}$ $\alpha = -1.3$ | | |

Table 2: Simulation of LF bins. The columns show the values: (1) $H\alpha$ luminosity in erg $s^{-1}$ (logarithmic scale); (2) number of emitters in the experiment; (3) number of emitters in the simulation

| log L(H$\alpha$) (1) | # galaxies exp (2) | # galaxies sim (3) |
|---|---|---|
| 39.75 | 7 ± 2.6 | 12.84 |
| 40.15 | 11 ± 3.3 | 9.73 |
| 40.55 | 9 ± 3 | 7.36 |
| 40.95 | 9 ± 3 | 5.54 |
| 41.35 | 3 ± 1.7 | 4.13 |
| 41.75 | 0 | 2.99 |
| 42.15 | 0 | 2.02 |
| 42.55 | 0 | 1.15 |

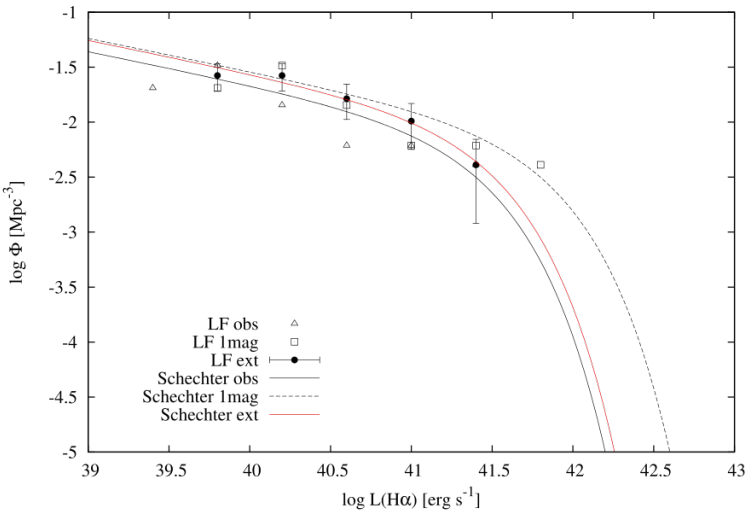


Figure 3: Extinction corrected LF with a Schechter function fit. It is compared with the previous LF calculations: observed LF and 1 mag extinction corrected LF.

### 4.1.2. Bright-end corrected luminosity function

We use Sloan Digital Sky Survey (SDSS) Legacy Survey data to try to get more galaxies for the bright-end of our study. We made this decision because, although the redshift range in this study is not widely explored by SDSS, we just need a sample of galaxies corresponding to the brightest bins. SDSS could provide the spectroscopic information we require. We employ the Data Release 8 (DR8) (Aihara et al., 2011). Particularly, we are interested in the spectroscopic galaxy products that the Max Planck Institute for Astrophysics and the Johns Hopkins University (MPA-JHU) provide, as we need the measurement of the $H\alpha$ line flux. We develop a series of Python scripts to get the appropriate data from the spectroscopic catalog, extracting the galaxies in our redshift bin that satisfies an equivalent width $EW(H\alpha{+}[NII]) > 10\,\text{Å}$. The resulting sample contains a total of 41 galaxies. This number is insufficient for our purpose so we adopt a different approach to solve it (Figure 4).

In the first place, we calculate the faint-end slope of the LF employing the points that are expected to follow a linear relation. In this case, we utilize the first four bins. The result of the fitting is $\alpha = -1.34 \pm 0.10$. Secondly, we employ the SFRd evolution equation (Villar et al., 2008):

$$SFRd = A(1+z)^{3.8} \tag{12}$$

Knowing that $SFRd(z = 0.84) = 0.19$ (Villar et al., 2008), we get a value of the constant $A = 0.017$. After that, we can predict a $SFRd(z = 0.61) = 0.1023$. Assuming that the change in the SFRd evolution through the cosmic history is not due to a change in the number of objects from z=0.84 to z=0.61, we can fix the value of the parameter $\phi^* = 10^{-2.76}\,\text{Mpc}^{-3}$.

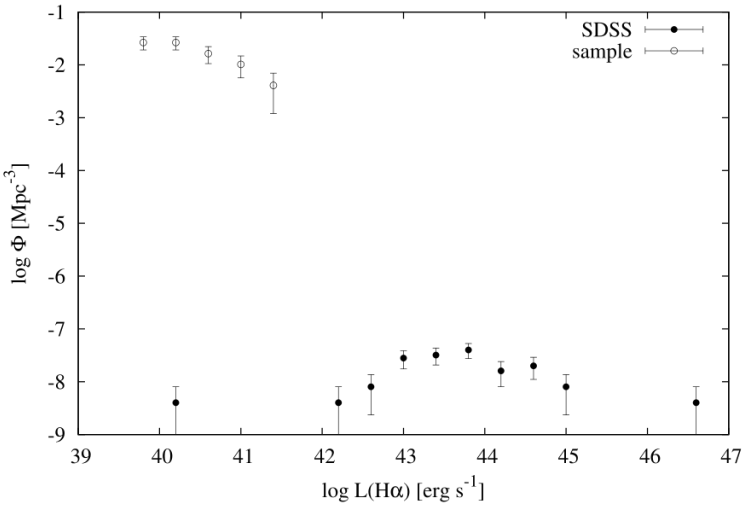


Figure 4: Extinction corrected LF along with extinction corrected bright-end obtained from SDSS data.

Having the knowledge of $\alpha$ and $\phi^*$ we can determine $L^*$ through the SFRd(z=0.61) prediction, since these three magnitudes are related as we will explain in the Section 4.2. The resulting characteristic luminosity is $L^* = 10^{42.74}\,\mathrm{erg\ s^{-1}}$.

Once we have the three parameters of the Schechter function that we expect for a redshift z=0.61, we can simulate those bins for which we have insufficient data, the brighter ones. After that, combining the faint-end bins obtained from the deep observations and the simulated ones, we fit the final LF to the Schechter function. In Figure 5 we plot the outcome of this approach and the numerical values are included in the Table 3. The derived fitting parameters are:

$$\phi^* = 10^{-2.77\pm0.05}\,\mathrm{Mpc^{-3}}$$

$$L^* = 10^{42.78\pm0.02}\,\mathrm{erg\ s^{-1}}$$

$$\alpha = -1.29 \pm 0.02$$

### 4.1.3. Comparation with other studies

We can compare this result with some other $H\alpha$ studies at different redshifts. In Figure 6 we can see how this study follows the trend with redshift marked by similar research. It is located between LFs at z = 0.84 and z = 0.4. Our study is much more deep than the other ones, reaching a limiting luminosity of $\log L(H\alpha) = 39.4\,\mathrm{erg\ s^{-1}}$, while the deepest one of other studies is Gallego et al. (1995) with a limiting luminosity of $\log L(H\alpha) = 40.4\,\mathrm{erg\ s^{-1}}$. We reach intrinsically less luminous galaxies even when we are at higher redshift.

Table 3: Extinction corrected LF derived from a combination of our data with the simulations. The columns show the values: (1) $H\alpha$ luminosity in erg s$^{-1}$ (logarithmic scale); (2) density of emitters in Mpc$^{-3}$ (logarithmic scale); (3) number of emitters

| log L(H$\alpha$) (1) | log $\phi$ (2) | # galaxies (3) |
|---|---|---|
| 39.8 | -1.58 ± 0.14 | 13 ± 3.6 |
| 40.2 | -1.58 ± 0.14 | 13 ± 3.6 |
| 40.6 | -1.79 ± 0.19 | 8 ± 2.8 |
| 41.0 | -1.99 ± 0.26 | 5 ± 2.2 |
| 41.4 | -1.96 | 5.36 |
| 41.8 | -2.13 | 3.65 |
| 42.2 | -2.34 | 2.25 |
| 42.6 | -2.66 | 1.07 |
| 43.0 | -3.24 | 0.28 |
| 43.4 | -4.37 | 0.02 |

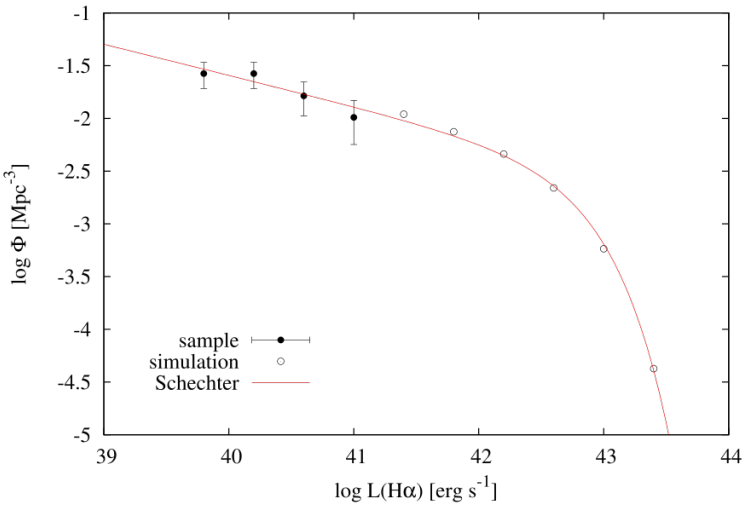


Figure 5: LF and Schechter fit derived from a combination of our faint-end points and a simulation of the bright-end points.

## 4.2. Star formation rate density

Having the LF and its Schechter parameters from the fitting, we can compute the $H\alpha$ luminosity density through:

$$\rho_L\left(H\alpha\right) = \phi^* L^* \Gamma\left(2+\alpha\right) \tag{13}$$

This result can be converted to star formation rate density through the Kennicutt (1998) calibration.

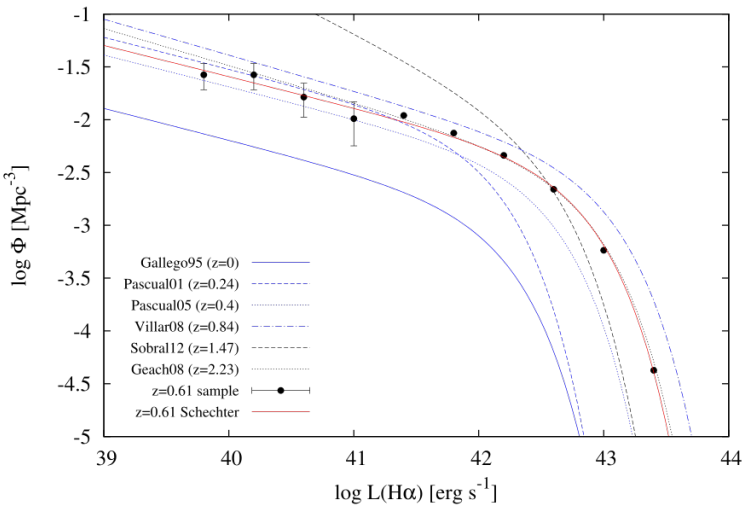


Figure 6: Comparation with similar $H\alpha$ studies: Gallego et al. (1995), Pascual et al. (2001), Pascual (2005), Sobral et al. (2012), Geach et al. (2008) as it is indicated in the legend.

$$SFR\left(M_{\odot}yr^{-1}\right) = 7.9 \times 10^{-42} L\left(H\alpha\right)\left(erg\ s^{-1}\right) \tag{14}$$

Then, the SFRd is simply:

$$SFRd\left(M_{\odot}yr^{-1}Mpc^{-3}\right) = 7.9 \times 10^{-42} \rho_L\left(H\alpha\right)\left(erg\ s^{-1}Mpc^{-3}\right) \tag{15}$$

We obtain the star formation rate for each galaxy. The results are shown in the Appendix A. The luminosity density and the SFRd derived from our Schechter parameters are:

$$\rho_L\left(H\alpha\right) = 10^{40.12\pm0.05}\ \text{erg s}^{-1}\text{Mpc}^{-3}$$

$$SFRd = (0.10 \pm 0.01)\ \ \text{M}_{\odot}\ \text{yr}^{-1}\text{Mpc}^{-3}$$

This result is checked from the AGNs contribution. We perform a search in the Chandra Deep Field South (CDFS) through the 2Ms source catalogs (Luo et al., 2008). Particularly we look for them in the Main Chandra Catalog, in the Supplementary CDFS plus ECDFS (Extended Chandra Deep Field South) Catalog and in the Supplementary Optically Bright Chandra Catalog (tables 2,5,6). The result is negative, no counterparts are observed for the objects in our sample.

We compare our result with other SFRd measured via $H\alpha$ line flux in Figure 7. The result of this work responds to the trend of previous researches. It follows the linear growth from the local Universe to z$\sim$1, particularly the growth marked by similar $H\alpha$ studies.

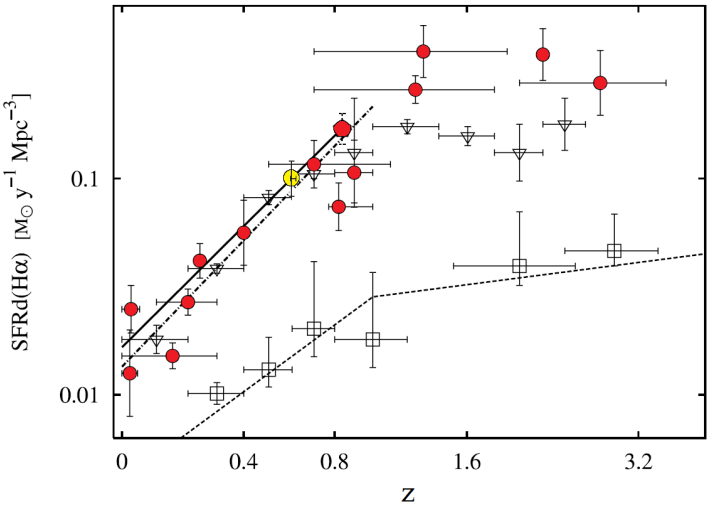


Figure 7: Adaptation of the figure from Villar et al. (2008). SFRd evolution with redshift based on $H\alpha$, IR and FUV. The result of this project is included as a yellow circle. Other measurements in $H\alpha$ (red circles) correspond to Gallego et al. (1995), Pérez-González et al. (2003), Sullivan et al. (2000), Pascual (2005), Villar et al. (2008), Tresse & Maddox (1998), Tresse et al. (2002), Doherty et al. (2006), Glazebrook et al. (1999), Yan et al. (1999), Hopkins et al. (2000), Moorwood et al. (2000), Pettini et al. (2001). IR measurements (triangles) (Pérez-González et al., 2005) and UV estimations in FUV (squares) (Schiminovich et al., 2005) are also shown. The derived evolution is included as a thick line, a dashed line for the FUV and a dashed-dot line for the IR. SFRd is corrected for reddening, while the UV values are not.

### 4.3. Spacial distribution

To have a preliminary idea about the clustering of the SFR at z=0.6, in this section we study the spacial distribution of the $H\alpha$ emitters in a qualitative approach.

We focus on the distribution in terms of the R-band apparent magnitude and the SFR (Figure 8). The objective is to figure out if the galaxies are gathered or located randomly. With the SFR we can also know if this magnitude is spread uniformly or there are regions dominated by this phenomenon.

Analyzing the images, we can see that there are some preferable regions where the galaxies are located. These regions are also places where star formation is higher, indicating a possible interaction phenomena that triggers it.

## 5. Physical properties

It is very interesting to study the properties of galaxies and their mutual relations. This allows us to understand the mechanisms and processes that occur in them, and to understand the differences between galaxies with intense star formation and other galaxies that evolve passively.

In this section we discard the 8 objects morphologically classified as "Uncertain" in Section 6. We are going to focus on individual physical properties and extract results from the analysis

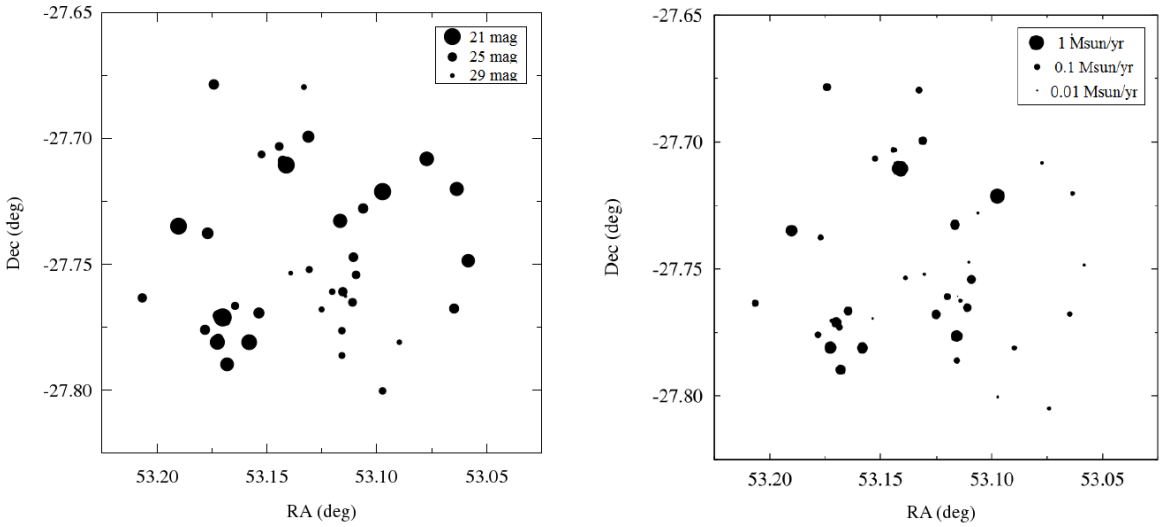


Figure 8: Spacial distribution of the sample. Left: the size of the point is related with apparent R magnitude. Right: the size of the point depend on the SFR.

of the effects that individual objects have in the whole sample. Thus, we remove these objects in order to avoid biased interpretations caused by low signal candidates. We have checked the consistency of the extracted overall results in the previous sections removing these objects.

## 5.1. Extinction and star formation

One of the properties we can study is extinction. In Section 3.3 we have shown how to calculate the $H\alpha$ extinction ( $A_{H\alpha}$ ). In Figure 9 we present an histogram. We see that most of the values are below 1 mag. The mean value is 0.77 mag and the deviation is 0.65 mag. This result is below those obtained in similar studies. In UCM Survey at z=0 (Gallego et al., 1995) the mean is $\sim$1 mag while at z=0.84 is 1.48 mag (Villar et al., 2008). Our result is in apparent contradiction, but we must always keep in mind the selection effects. We are sampling a population of UV-bright low-mass galaxies, completely different from those in the other studies, so we do not expect to follow an evolution relation with redshift between different populations.

Previously, we have also obtained the extinction corrected SFR. These two quantities are related as we can see in Figure 10. The more the SFR the greater the obscuration. This effect is also seen in other samples, locally at z=0 and in less evolved populations at z=0.84. The peculiarity of our sample is evident in this graph. We see, as in the other two studies, there is an apparent linear relation. However, the selection effects cause differences. The objects of this work that overlap with the characteristics of the z=0.84 galaxies are disks. The remaining objects plotted at z=0.61 trace a different galaxy population. Our survey cover a deep and small field, then, we do not see many disks due to a lack of area and we see a high number of small galaxies with low SFR.

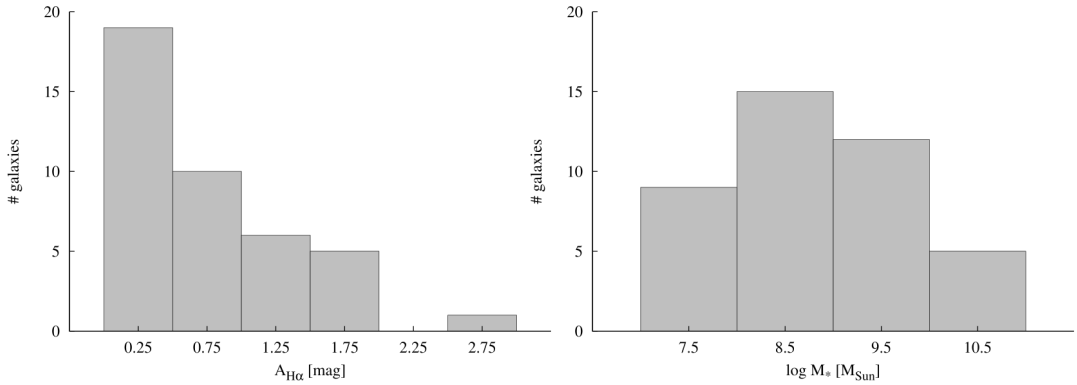


Figure 9: Left: histogram of the $H\alpha$ extinction. Right: histogram of the mass. In the Appendix A individual values for each galaxy can be consulted.

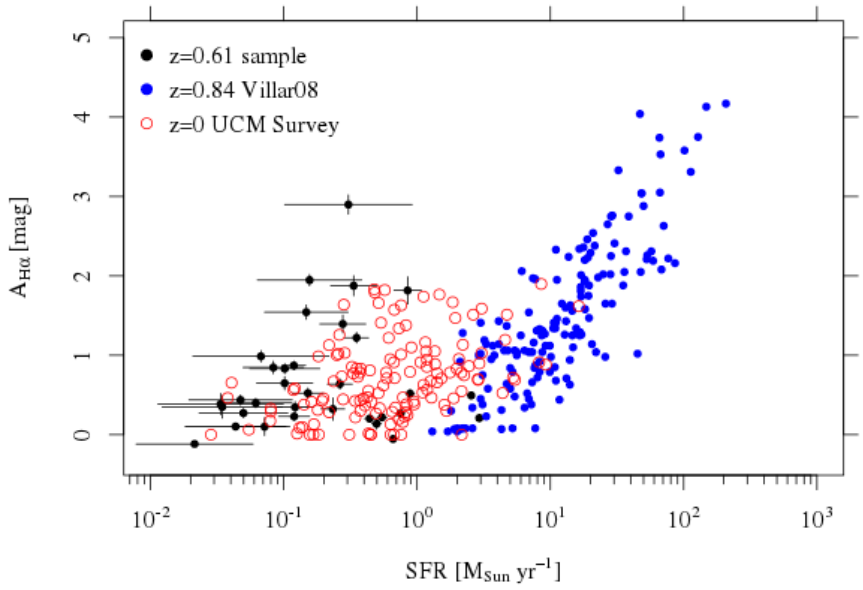


Figure 10: $H\alpha$ extinction versus star formation rate. This work is shown along with UCM Survey (z=0) and Villar et al. (2008) (z=0.84). The plot shows clearly how different are the three populations in terms of SFR.

## 5.2. Mass and star formation

Moreover, one of the most important properties that we can study in galaxies is their stellar mass. This quantity tells us the amount of gas transformed into stars over their existence. As a global property it is also interesting, as it provides information about the evolution of the Universe. In this work we take the stellar masses from the CANDELS project. In Figure 9

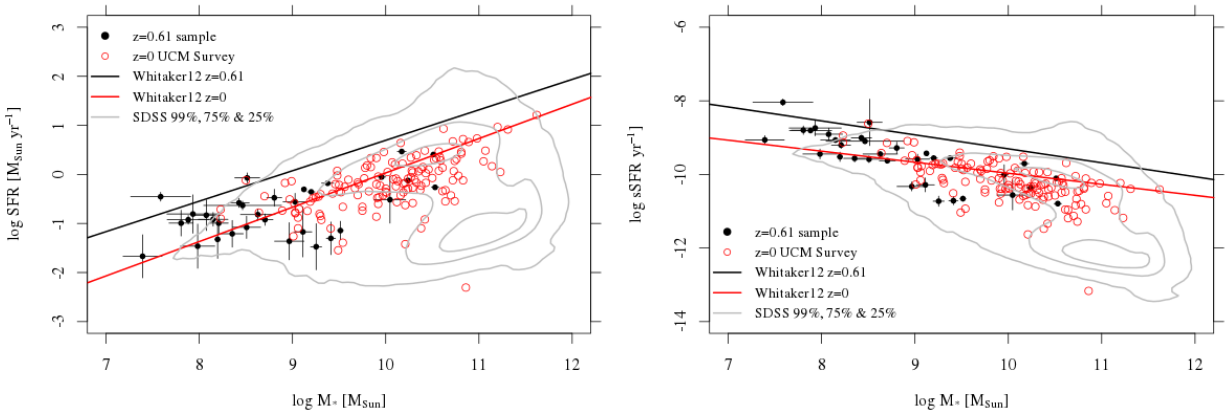


Figure 11: $H\alpha$ Left: star formation rate versus stellar mass. Right: specific star formation rate versus mass.

we show a histogram of our sample. We can see that the majority of the objects are below $10^9\,M_\odot$. In Figure 11 we show the extinction corrected SFR as a function of mass. We see a correlation between the two magnitudes. The galaxies with higher star formation are the ones with higher mass. This trend has been studied in depth (Noeske et al., 2007; Rodighiero et al., 2011; Whitaker et al., 2012) and it is known as the main sequence of star-forming galaxies. We include in the plot the main sequence for z=0.61 given by Whitaker et al. (2012). We see that our objects are below the expected trend. We interpret this as a consequence of the galaxy population we are observing. They are UV-bright very low-mass galaxies, much less massive than those in Whitaker et al. (2012), so we are seeing a different population. We also use a selection criteria $EW(H\alpha + [NII]) > 10\,\text{Å}$, so we see galaxies forming fewer stars than those in the other studies. In this plot we include the UCM Survey at z=0, the main sequence of SFGs at this redshift and the contours of SDSS galaxies as a reference in the local Universe. We can see there is an offset between both of them, so for a given mass, the SFGs in the Universe at z=0.61 have more formation than those in the local Universe. In other words, galaxies with similar formation are more massive at z=0 than at higher redshifts. However, it is more convenient to study this not in absolute terms of SFR, but in terms of the specific star formation rate (sSFR), ie, the SFR divided by the stellar mass of the galaxy. Thus, we study the contribution of the SFR in the galaxy where it happens. In this sense we represent the sSFR as a function of mass (Figure 11). In this case we find that the sSFR decreases with mass. The less massive galaxies are subjected to a more drastic effect for their evolution. In terms of the redshift we observe that, for the same specific star formation, galaxies are more massive at higher redshifts. This phenomenon is known as downsizing (Cowie et al., 1996). As the story of the Universe progresses, star formation has its influence in less massive galaxies. The majority of the galaxy mass is formed at high redshifts.

# 6. Morphology

Using CANDELS archive we generate RGB (Red-Green-Blue) images. We employ three filters of the Advanced Camera for Surveys (ACS) of *HST*. In the Table 4 it is shown the colour/filter assignments along with the observed and rest-frame wavelengths for each filter. In this configuration, at rest-frame we are observing in the spectral range of NUV, B and V bands, therefore we draw regions associated with star formation, young populations, with B and V filters (blue and green colours in the pictures). The filter z (red colour) shows a more evolved population. The combined action of the three filters trace both star-forming and evolved regions. We can develop a morphological classification.

Table 4: Colour/filter assignments along with the observed and rest-frame wavelengths for each filter employed in the RGB images.

| Colour | Filter | $\lambda_{obs}$ [nm] | $\lambda_{rf}$ [nm] |
|---|---|---|---|
| Blue | B (FW435) | 435 | 270 |
| Green | V (FW606) | 606 | 376 |
| Red | z (FW850) | 850 | 528 |

For some objects of the sample we have adopted a slightly different approach. We search in the II/258 Hubble Ultra Deep Field Catalog (UDF) (Beckwith, 2005), founding 11 results. We can use the UDF SkyWalker [2] tool to create images with greater exposure. The filters used in this case are similar: ACS F435W (B), F606W (V), F775W (i), F850LP (z). All RGB images are presented in Appendix B.

Our classification is based in the following classes:

- Spirals + HII regions. Spiral galaxies where we observe HII regions associated with intense star formation in blue.
- Disk galaxies. Those having a disk, but no spiral structure.
- Irregulars. Galaxies with irregular morphology.
- Blue Compact Dwarf (BCD). Compact galaxies showing blue colour and ellipsoidal morphology with a lot of gas and recient star formation.
- Uncertain. We include those objects with a too low signal that can not be distinguished of the background.

We can now perform a study of the physical properties in these categories. In particular, we focus on rest-frame $EW(H\alpha)$, $(H\alpha)$ extinction, SFR, sSFR, stellar mass and size. In Table 6 we show the results of these parameters depending on the morphological class. The values correspond to the average and standard deviation of the studied property for a particular galaxy category. We can see that for this sample *Spirals + HII regions* are the largest and most massive with a higher SFR. *Disk galaxies* are smaller than previous ones and have lower SFR.

[2] http://www.aip.de/groups/galaxies/sw/udf/swudfV1.0.html

Table 5: Amount of galaxies in each category.

| Category | Number |
|---|---|
| Spirals + HII regions | 6(15%) |
| Disk galaxies | 5(12%) |
| Irregulars | 13(32%) |
| BCD | 9(22%) |
| Uncertain | 8(19%) |

We can interpret them as a small version of the first ones. *BCD* are very compact and low-mass galaxies, however they have a high SFR for its size, much larger than *Irregulars* and similar to *Disk galaxies* that are much larger and more massive. As for the objects of the category *Uncertain*, they present unreliable results. Apart from this, we observe a growing relation in extinction with the morphological category form *Spirals + HII regions* to *BCD*. The last ones evidence a strong star formation environment, showing sSFR very high and close to those in *Spirals + HII regions*. *BCD* are compact, low-mass and starburst systems.

Table 6: Physical properties for our morphological categories. The columns show the values: (1) category; (2) rest-frame equivalent width in Å; (3) $H\alpha$ extinction in magnitudes; (4) extinction corrected star formation rate in $M_\odot\,yr^{-1}$; (5) extinction corrected specific star formation rate in $Gyr^{-1}$; (6) stellar mass in $\log M_\odot$; (7) diameter in kpc.

| Category (1) | $EW_{rf}$ (2) | $A_{H\alpha}$ (3) | $SFR_{cor}$ (4) | $sSFR_{cor}$ (5) | Mass (6) | Diameter (7) |
|---|---|---|---|---|---|---|
| Spirals + HII regions | 27±16 | 0.28±0.19 | 1.4±1.1 | 4.8±7.8 | 9.4±1.1 | 15.3±5.3 |
| Disk galaxies | 20±16 | 0.56±0.59 | 0.27±0.20 | 1.1±2.0 | 8.95±0.57 | 13.2±7.3 |
| Irregulars | 34±31 | 0.69±0.81 | 0.11±0.10 | 0.9±1.8 | 8.82±0.81 | 8.6±4.0 |
| BCD | 156±190 | 1.06±0.61 | 0.26±0.24 | 3.0±3.9 | 8.07±0.54 | 4.9±1.6 |
| Uncertain | 567±1100 | 1.08±0.43 | 0.095±0.051 | 0.8±1.5 | 8.68±0.78 | 5.5±2.9 |

# 7. Spectroscopy

In this section we are going to show the outcome obtained through spectra analysis. As we have described in Section 2, we have collected a sample of 8 spectra for 7 different objects that can be consulted in Appendix C. Making use of the software IRAF and the task *splot* we measure the emission lines for each spectrum. In particular, we perform ten measurements for each line we can identify, taking flux, EW and FWHM. We want to find out the spectroscopic classification of each object. Those galaxies with high $[OIII]/H\beta$ ratio, $EW(H\alpha)$, $EW(H\beta)$, $EW([OII])$ and low masses and sizes are classified as *HII-like*. Galaxies with low $[OIII]/H\beta$ ratio, $EW(H\alpha)$, $EW(H\beta)$, $EW([OII])$ and high masses and sizes are classified as *Disk-like*. We add a third category for *Disk-like* galaxies with low masses, *Dwarf disk-like* galaxies.

Apart form this, it is vey useful to plot some line-ratio diagnostic diagrams (Baldwin et al., 1981; Veilleux & Osterbrock, 1987). We focus the analysis on two diagrams: excitation versus luminosity and rest frame $EW([OII])$ versus luminosity (Figure 12). These diagrams are

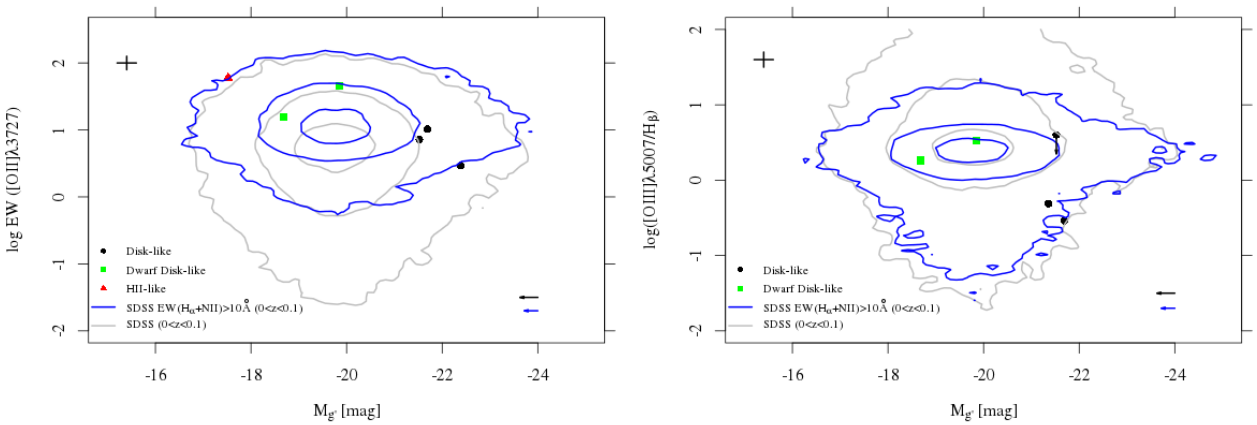


Figure 12: Left: excitation versus rest frame absolute g' magnitude. Right: $EW([OII])$ versus rest frame absolute g' magnitude. Spectroscopic classification is included as explained in the legend as well as the SDSS reference (gray contours 99%,75% and 25%). An estimation of the error is shown at the top left corner of each image. At the bottom right corner two arrows indicate the displacement considering rest frame B absolute magnitude instead of g' for the sample points (black arrow) and for the SDSS contours (blue arrow). The length is established through a typical galaxy color (Fukugita et al., 1995).

common in this kind of studies (Gallego et al., 1997; Guzmán et al., 1997). The first one provide information about excitation and metallicity of the gas and the second one is related with SFR, as [OII] luminosity is a good tracer of this magnitude. We add a reference to SDSS data in this plots. To achieve this, we develop a series of scripts in Pyhton language to collect all the spectroscopic data in SDSS DR8 spectroscopic catalog that fits our critea. We cross-match our resulting samples with the desirable tables in SDSS through SQL queries using CasJobs platform. Two references are included in each graph. Galaxies in the redshift bin $0.0 < z < 0.1$ and galaxies in this bin but with $EW(H\alpha + [NII]) > 10\,\text{Å}$. It is not possible to get B band absolute magnitudes ( $M_B$ ) for the SDSS galaxies, as this is not a SDSS band, so we decide to plot $M_{g'}$ instead. The HII-like galaxy appear in the first diagram but not in the second due to a poor signal spectrum that do not permit to measure the lines. EW for recombination line $H\beta$ is corrected form self-absorption (2Å).

We see that *HII-like* galaxies present higher excitation and lower luminosities. On the contrary, *Disk-like* ones present lower excitation but higher luminosities. *Dwarf disk-like* type are located in a transition between this two types. These differences are also seen in the second graph, as *HII-like* ones show higher $EW([OII])$ than *Disk-like*.

# 8. Results and conclusions

In this work we have studied a sample of 41 galaxies with active star formation at z$\sim$0.61 selected by their emission in $H\alpha$ in ultradeep images (32h exposure time) taken with a narrow-band filter in the near-infrared with HAWK-I instrument on the VLT. The aim is to characterize the physical and global properties of this sample of galaxies.

Firstly, we have undertaken an investigation of the photo-z provided by CANDELS. We have found that $\sim$90% of the sample corresponds to $H\alpha$ real emitters.

Then, we have calculated the luminosity function corrected from extinction, fitting to a Schechter function with parameters: $\phi^* = 10^{-2.77\pm0.05}\,\mathrm{Mpc}^{-3}$, $L^* = 10^{42.78\pm0.02}\,\mathrm{erg\ s}^{-1}$ and $\alpha = -1.29\pm0.02$. The determination of the $\alpha$ parameter is the deepest to date in similar studies for the LF faint-end. This leads to a determination of the $SFRd = (0.10 \pm 0.01)\ \mathrm{M}_\odot\,\mathrm{yr}^{-1}\mathrm{Mpc}^{-3}$. We conclude that this result confirms the growth from the local Universe to z$\sim$1.

Previously, we have tried to get the points of the LF bright-end through SDSS data without results. We conclude that SDSS can not be used to obtain the bright-end at z$\sim$0.61.

The spatial distribution of galaxies shows regions of clustering increasing the SFR and decreasing it in more isolated galaxies. We conclude that the SFR increases with the presence of nearby galaxies.

The galaxies in the sample have a mean extinction of 0.77 mag. This value does not correspond to those expected from other studies due to selection effects, since we are not considering the same type of galaxies.

On the other hand, we have found a correlation between extinction and SFR. We conclude that galaxies have higher extinction with increasing SFR.

We have found a correlation between SFR and stellar mass. As the mass increases so does the SFR. Our objects are below the main sequence of (Whitaker et al., 2012) due to selection effects in the sample, since we consider UV-bright galaxies with low masses. In terms of redshift, we conclude that for a given mass, the SFGs at z=0.61 are more star-forming than those in the local Universe. In other words, with a similar formation, galaxies are more massive in the local Universe than at greater z.

In terms of the specific star formation rate the correlation is negative. With increasing stellar mass sSFR decreases. Considering the redshift, we conclude that for a given sSFR, star formation is found in less massive galaxies with decreasing z, evidence of downsizing. The influence of star formation in low-mass galaxies will become higher with decreasing z. The majority of the galaxy mass is formed at high z.

According to our morphological classification 27% of the sample are disks (*Spirals+HII regions* and *Disk galaxies*), 32% are *Irregulars* and 22% *BCD*. A 19% are *Uncertain*, for which we can not establish visual classification. We conclude that disks have the higher values of SFR, but in terms of sSFR, *BCD* form stars at the same rate.

Finally, spectroscopic study shows a galaxy *HII-like*, two *Dwarf disk-like* galaxies and three *Disk-like* galaxies. We conclude that excitation decreases and luminosity increases with the spectroscopic class.

## Future work

To continue this work we will make an estimate of the star formation histories (SFH) of the objects in the sample. In addition, we will expand the number of galaxies using observations form the ALHAMBRA Survey (Moles et al., 2008). The results will be published in a peer-reviewed journal.

Furthermore, we are going to continue the study in the line of dwarf galaxies with granted observing time in GTC/OSIRIS.

## References

Aihara, H., Allende Prieto, C., An, D., et al. 2011, ApJS, 193, 29

An, F. X., Zheng, X. Z., Wang, W.-H., et al. 2014, ApJ, 784, 152

Baldwin, J. A., Phillips, M. M., & Terlevich, R. 1981, PASP, 93, 5

Balestra, I., Mainieri, V., Popesso, P., et al. 2010, A&A, 512, A12

Barro, G., Pérez-González, P. G., Gallego, J., et al. 2011, ApJS, 193, 13

Beckwith, S. V. W. 2005, VizieR Online Data Catalog, 2258, 0

Buat, V., Iglesias-Páramo, J., Seibert, M., et al. 2005, ApJ, 619, L51

Calzetti, D., Armus, L., Bohlin, R. C., et al. 2000, ApJ, 533, 682

Clément, B., Cuby, J.-G., Courbin, F., et al. 2012, A&A, 538, A66

Cowie, L. L., Songaila, A., Hu, E. M., & Cohen, J. G. 1996, AJ, 112, 839

Dahlen, T., Mobasher, B., Dickinson, M., et al. 2010, ApJ, 724, 425

Doherty, M., Bunker, A., Sharp, R., et al. 2006, MNRAS, 370, 331

Fukugita, M., Shimasaku, K., & Ichikawa, T. 1995, PASP, 107, 945

Gallego, J., Zamorano, J., Aragon-Salamanca, A., & Rego, M. 1995, ApJ, 455, L1

Gallego, J., Zamorano, J., Rego, M., & Vitores, A. G. 1997, ApJ, 475, 502

Geach, J. E., Smail, I., Best, P. N., et al. 2008, MNRAS, 388, 1473

Glazebrook, K., Blake, C., Economou, F., Lilly, S., & Colless, M. 1999, MNRAS, 306, 843

Gómez Guijarro, C. 2013, e-print UCM, Cod 23208, TAD

Grogin, N. A., Kocevski, D. D., Faber, S. M., et al. 2011, ApJS, 197, 35

Guo, Y., Ferguson, H. C., Giavalisco, M., et al. 2013, ApJS, 207, 24

Guzmán, R., Gallego, J., Koo, D. C., et al. 1997, ApJ, 489, 559

Hopkins, A. M., & Beacom, J. F. 2006, ApJ, 651, 142

Hopkins, A. M., Connolly, A. J., & Szalay, A. S. 2000, AJ, 120, 2843

Kantowski, R., Kao, J. K., & Thomas, R. C. 2000, ApJ, 545, 549

Kennicutt, R. C., & Evans, N. J. 2012, ARA&A, 50, 531

Kennicutt, Jr., R. C. 1998, ARA&A, 36, 189

Kissler-Patig, M., Pirard, J.-F., Casali, M., et al. 2008, A&A, 491, 941

Koekemoer, A. M., Faber, S. M., Ferguson, H. C., et al. 2011, ApJS, 197, 36

Le Fèvre, O., Vettolani, G., Paltani, S., et al. 2004, A&A, 428, 1043

Luo, B., Bauer, F. E., Brandt, W. N., et al. 2008, ApJS, 179, 19

Madau, P., & Dickinson, M. 2014, ArXiv e-prints, arXiv:1403.0007

Madau, P., Ferguson, H. C., Dickinson, M. E., et al. 1996, MNRAS, 283, 1388

Moles, M., Benítez, N., Aguerri, J. A. L., et al. 2008, AJ, 136, 1325

Moorwood, A. F. M., van der Werf, P. P., Cuby, J. G., & Oliva, E. 2000, A&A, 362, 9

Muñoz-Mateos, J. C., Gil de Paz, A., Boissier, S., et al. 2009, ApJ, 701, 1965

Noeske, K. G., Weiner, B. J., Faber, S. M., et al. 2007, ApJ, 660, L43

Pascual, S. 2005, PASP, 117, 120

Pascual, S., Gallego, J., Aragón-Salamanca, A., & Zamorano, J. 2001, A&A, 379, 798

Pascual, S., Gallego, J., & Zamorano, J. 2007, PASP, 119, 30

Pérez-González, P. G., Zamorano, J., Gallego, J., Aragón-Salamanca, A., & Gil de Paz, A. 2003, ApJ, 591, 827

Pérez-González, P. G., Rieke, G. H., Egami, E., et al. 2005, ApJ, 630, 82

Pettini, M., Shapley, A. E., Steidel, C. C., et al. 2001, ApJ, 554, 981

Rodighiero, G., Daddi, E., Baronchelli, I., et al. 2011, ApJ, 739, L40

Schechter, P. 1976, ApJ, 203, 297

Schiminovich, D., Ilbert, O., Arnouts, S., et al. 2005, ApJ, 619, L47

Schlafly, E. F., & Finkbeiner, D. P. 2011, ApJ, 737, 103

Schmidt, M. 1968, ApJ, 151, 393

Siebenmorgen, R., Carraro, G., Valenti, E., et al. 2011, The Messenger, 144, 9

Sobral, D., Best, P. N., Matsuda, Y., et al. 2012, MNRAS, 420, 1926

Sullivan, M., Treyer, M. A., Ellis, R. S., et al. 2000, MNRAS, 312, 442

Tresse, L., & Maddox, S. J. 1998, ApJ, 495, 691

Tresse, L., Maddox, S. J., Le Fèvre, O., & Cuby, J.-G. 2002, MNRAS, 337, 369

Vanzella, E., Cristiani, S., Dickinson, M., et al. 2008, A&A, 478, 83

Veilleux, S., & Osterbrock, D. E. 1987, ApJS, 63, 295

Villar, V., Gallego, J., Pérez-González, P. G., et al. 2008, ApJ, 677, 169

Whitaker, K. E., van Dokkum, P. G., Brammer, G., & Franx, M. 2012, ApJ, 754, L29

Yan, L., McCarthy, P. J., Freudling, W., et al. 1999, ApJ, 519, L47

# Appendices

# A. Sample properties

Table 7: Measurements of the 46 galaxies in the raw sample. The columns show the values: (1) CANDELS ID. (2) RA(J2000) from CANDELS (deg). (3) Dec(J2000) from CANDELS (deg). (4) Original ID. (5) RA(J2000) Original (deg). (6) Dec(J2000) Original (deg). (7) Line flux ( $10^{-18}$erg s$^{-1}$cm$^{-2}$). (8) Continuum flux ( $10^{-20}$erg s$^{-1}$cm$^{-2}$Å$^{-1}$)

| CANDELS ID (1) | $\alpha$(J2000) (2) | $\delta$(J2000) (3) | Original ID (4) | $\alpha$(J2000) (5) | $\delta$(J2000) (6) | $f_l$ (7) | $f_C$ (8) |
|---|---|---|---|---|---|---|---|
| 11513 | 53.074157 | -27.804923 | HAWKI0000773 | 53.074116 | -27.804887 | 2.4 ± 1.7 | 2.1 ± 2.0 |
| 12039 | 53.097336 | -27.800426 | HAWKI0000694 | 53.097350 | -27.800418 | 2.7 ± 0.5 | 0.3 ± 0.1 |
| 13781 | 53.168017 | -27.789670 | HAWKI0000310 | 53.168020 | -27.789668 | 34.5 ± 2.0 | 54.1 ± 2.3 |
| 14122 | 53.115761 | -27.786059 | HAWKI0000971 | 53.115789 | -27.786055 | 3.3 ± 1.6 | 1.5 ± 1.9 |
| 15282 | 53.158169 | -27.781095 | HAWKI0000670 | 53.158202 | -27.781076 | 54.5 ± 2.2 | 71.6 ± 2.6 |
| 15286 | 53.172260 | -27.779516 | HAWKI0000620 | 53.172260 | -27.779516 | 3.5 ± 2.2 | 9.1 ± 2.5 |
| 15398 | 53.172609 | -27.780967 | HAWKI0000521 | 53.172612 | -27.780954 | 43.3 ± 2.4 | 119.8 ± 2.9 |
| 15650 | 53.115894 | -27.776418 | HAWKI0001293 | 53.115899 | -27.776413 | 13.0 ± 2.3 | 5.4 ± 2.7 |
| 15784 | 53.178185 | -27.775894 | HAWKI0000675 | 53.178175 | -27.775884 | 2.9 ± 2.1 | 8.8 ± 2.3 |
| 16155 | 53.168582 | -27.772930 | HAWKI0000850 | 53.168568 | -27.772921 | 2.1 ± 1.9 | 3.2 ± 2.2 |
| 16483 | 53.160006 | -27.771002 | HAWKI0001000 | 53.160026 | -27.771008 | 2.4 ± 1.8 | 4.4 ± 2.2 |
| 16644 | 53.172101 | -27.770380 | HAWKI0000899 | 53.172105 | -27.770372 | 2.2 ± 2.6 | 26.3 ± 3.1 |
| 16798 | 53.125143 | -27.767847 | HAWKI0001494 | 53.125131 | -27.767849 | 9.3 ± 1.8 | 2.6 ± 2.1 |
| 16839 | 53.153536 | -27.769445 | HAWKI0001134 | 53.153533 | -27.769445 | 1.9 ± 2.1 | 13.4 ± 2.4 |
| 16845 | 53.064759 | -27.767741 | HAWKI0002189 | 53.064762 | -27.767735 | 4.6 ± 2.2 | 6.9 ± 2.6 |
| 17058 | 53.169925 | -27.771024 | HAWKI0000783 | 53.169923 | -27.771022 | 34.8 ± 2.6 | 186.7 ± 3.1 |
| 17075 | 53.164651 | -27.766606 | HAWKI0001111 | 53.164645 | -27.766601 | 4.8 ± 1.8 | 2.8 ± 2.2 |
| 17183 | 53.111168 | -27.765216 | HAWKI0001733 | 53.111168 | -27.765221 | 12.0 ± 2.5 | 6.6 ± 2.9 |
| 17393 | 53.206666 | -27.763450 | HAWKI0000770 | 53.206633 | -27.763441 | 7.7 ± 2.0 | 12.3 ± 2.2 |
| 17503 | 53.114224 | -27.762464 | HAWKI0001810 | 53.114230 | -27.762454 | 2.0 ± 1.4 | 1.0 ± 1.5 |
| 17686 | 53.120235 | -27.760870 | HAWKI0001793 | 53.120249 | -27.760928 | 3.8 ± 1.0 | 0.1 ± 1.0 |
| 17704 | 53.115577 | -27.760782 | HAWKI0001856 | 53.115607 | -27.760795 | 1.9 ± 2.0 | 3.8 ± 2.3 |
| 18444 | 53.109247 | -27.754127 | HAWKI0002176 | 53.109242 | -27.754140 | 1.7 ± 1.9 | 4.2 ± 2.2 |
| 18482 | 53.139078 | -27.753542 | HAWKI0001845 | 53.139100 | -27.753533 | 3.1 ± 1.6 | 2.1 ± 1.9 |
| 18684 | 53.130594 | -27.752070 | HAWKI0001996 | 53.130651 | -27.752114 | 1.7 ± 1.7 | 2.6 ± 2.0 |
| 19214 | 53.058253 | -27.748481 | HAWKI0002871 | 53.058214 | -27.748477 | 3.2 ± 2.4 | 45.9 ± 2.9 |
| 19256 | 53.110459 | -27.747339 | HAWKI0002353 | 53.110461 | -27.747324 | 2.0 ± 2.1 | 5.0 ± 2.5 |
| 20380 | 53.177126 | -27.737653 | HAWKI0001993 | 53.177136 | -27.737653 | 7.9 ± 2.1 | 17.6 ± 2.3 |
| 20901 | 53.190161 | -27.734945 | HAWKI0001834 | 53.190155 | -27.734949 | 46.3 ± 2.8 | 198.6 ± 3.3 |
| 21046 | 53.116710 | -27.732614 | HAWKI0002795 | 53.116744 | -27.732602 | 28.6 ± 2.3 | 48.2 ± 2.7 |
| 21360 | 53.106294 | -27.727954 | HAWKI0003083 | 53.106289 | -27.727952 | 2.6 ± 2.3 | 9.6 ± 2.7 |

*-Continuation*

| CANDELS ID (1) | $\alpha$(J2000) (2) | $\delta$(J2000) (3) | Original ID (4) | $\alpha$(J2000) (5) | $\delta$(J2000) (6) | $f_l$ (7) | $f_C$ (8) |
|---|---|---|---|---|---|---|---|
| 22420 | 53.097519 | -27.721271 | HAWKI0003345 | 53.097508 | -27.721254 | 129.2 ± 2.4 | 374.5 ± 2.8 |
| 22556 | 53.063490 | -27.720247 | HAWKI0004063 | 53.063497 | -27.720264 | 5.3 ± 2.3 | 42.4 ± 2.7 |
| 22962 | 53.142643 | -27.708699 | HAWKI0004500 | 53.142589 | -27.708712 | 7.2 ± 2.3 | 5.0 ± 2.7 |
| 23065 | 53.152421 | -27.706515 | HAWKI0003342 | 53.152423 | -27.706500 | 4.4 ± 0.9 | 0.4 ± 0.1 |
| 23137 | 53.077383 | -27.708195 | HAWKI0004594 | 53.077372 | -27.708195 | 3.3 ± 2.9 | 50.8 ± 3.5 |
| 23248 | 53.141244 | -27.710543 | HAWKI0003255 | 53.141222 | -27.710531 | 189.8 ± 2.9 | 243.8 ± 3.5 |
| 24623 | 53.174256 | -27.678432 | HAWKI0004679 | 53.174291 | -27.678418 | 13.8 ± 2.2 | 13.2 ± 2.4 |
| 26132 | 53.131199 | -27.699450 | HAWKI0004281 | 53.131219 | -27.699445 | 6.0 ± 2.3 | 27.3 ± 2.7 |
| 26460 | 53.144189 | -27.703179 | HAWKI0004340 | 53.144176 | -27.703179 | 3.9 ± 2.3 | 4.2 ± 2.7 |
| 31370 | 53.089858 | -27.781079 | HAWKI0001413 | 53.089820 | -27.781228 | 1.8 ± 1.6 | 1.8 ± 1.8 |
| 34118 | 53.132941 | -27.679610 | HAWKI0003578 | 53.132942 | -27.679586 | 3.3 ± 1.6 | 1.3 ± 1.8 |
| - | - | - | HAWKI0003148 | 53.179710 | -27.702845 | 30.9 ± 2.2 | 5.2 ± 2.5 |
| - | - | - | HAWKI0003151 | 53.175771 | -27.704078 | 6.1 ± 1.9 | 4.9 ± 2.1 |
| - | - | - | HAWKI0003361 | 53.150852 | -27.667993 | 72.7 ± 2.6 | 382.6 ± 3.0 |
| - | - | - | HAWKI0003606 | 53.037469 | -27.710118 | 4.5 ± 0.6 | 0.4 ± 0.1 |

Table 8: Data taken from the CANDELS database of the 41 galaxies in the final sample along with the morphological classification. The columns show the values: (1) CANDELS ID. (2) Photometric redshift. (3) Spectroscopic redshift. (4) R-band apparent magnitude (mag). (5) Stellar mass ($\log M_{\odot}$). (6) Kron diameter (kpc). (7) Infrared luminosity (8-1000 $\mu$m) ($\log L_{\odot}$). (8) Observed FUV magnitude (mag). The mean error is 0.2 mag. (9) Observed NUV magnitude (mag). The mean error is 0.2 mag. (10) Morphological classification

| CANDELS ID | photo-z | spec-z | $m_R$ | Mass | Diameter | LIR | FUV | NUV | Morph |
|---|---|---|---|---|---|---|---|---|---|
| (1) | (2) | (3) | (4) | (5) | (6) | (7) | (8) | (9) | (10) |
| 11513 | 5.61±2.81 | - | - | 9.73±1.82 | 7.52 | - | 27.49 | 26.61 | Uncertain |
| 12039 | 4.18±2.10 | - | 26.68 | 9.56±0.06 | 4.24 | - | 26.34 | 26.20 | Uncertain |
| 13781 | 0.59±0.30 | 0.6190±0.0001 | 23.24 | 9.12±0.03 | 8.09 | 10.09±0.16 | 24.62 | 24.14 | Disk galaxies |
| 14122 | 1.65±0.83 | - | 27.00 | 8.82±0.06 | 4.10 | 11.02±0.04 | 27.37 | 27.28 | Uncertain |
| 15282 | 0.59±0.30 | 0.6200±0.0001 | 22.18 | 9.38±0.07 | 14.19 | 10.05±0.05 | 23.08 | 22.87 | Spirals+HII regions |
| 15286 | 0.65±0.33 | - | 25.34 | 8.35±0.12 | 7.05 | 10.09±0.09 | 26.10 | 26.08 | Irregulars |
| 15398 | 0.57±0.29 | 0.6190±0.0001 | 22.55 | 9.96±0.05 | 13.20 | 10.70±0.06 | 25.16 | 24.22 | Spirals+HII regions |
| 15650 | 1.13±0.57 | - | 26.70 | 8.51±0.13 | 5.13 | 11.84±0.21 | 27.08 | 26.68 | BCD |
| 15784 | 0.60±0.31 | - | 25.27 | 8.08±0.15 | 6.57 | 12.01±0.09 | 25.76 | 25.80 | BCD |
| 16155 | 0.56±0.29 | - | 26.55 | 7.93±0.28 | 4.71 | 11.66±0.05 | 27.95 | 27.62 | BCD |
| 16644 | 0.54±0.28 | - | 24.65 | 9.11±0.10 | 8.12 | 10.51±0.07 | 27.54 | 26.68 | Disk galaxies |
| 16798 | 1.42±0.72 | - | 27.47 | 7.59±0.32 | 3.37 | 10.95±0.05 | 27.29 | 27.01 | BCD |
| 16839 | 0.51±0.26 | - | 24.73 | 9.25±0.06 | 18.25 | 9.65±0.25 | 27.12 | 26.57 | Irregulars |
| 16845 | 0.66±0.34 | - | 25.31 | 8.21±0.10 | 4.94 | 10.56±0.12 | 26.07 | 25.94 | Irregulars |
| 17058 | 4.00±0.61 | 0.6218±0.0001 | 20.92 | 10.53±0.04 | 25.42 | 10.95±0.00 | 23.01 | 22.23 | Spirals+HII regions |
| 17075 | 1.65±0.83 | - | 26.35 | 8.81±0.08 | 7.38 | 12.13±0.14 | 26.54 | 26.23 | Irregulars |
| 17183 | 1.14±0.58 | - | 25.99 | 8.43±0.11 | 4.16 | 10.42±0.08 | 26.36 | 26.11 | BCD |
| 17393 | 1.08±0.55 | - | 25.74 | 8.63±0.19 | 4.63 | 10.33±0.09 | 26.07 | 25.91 | Irregulars |
| 17503 | 0.62±0.32 | - | 28.86 | 7.90±0.16 | 4.81 | 10.06±0.19 | 28.92 | 28.79 | Uncertain |
| 17686 | 1.79±0.90 | - | 27.19 | 7.18±0.10 | 3.37 | 10.97±0.06 | 27.70 | 27.84 | Uncertain |
| 17704 | 0.14±0.08 | - | 25.72 | 7.39±0.21 | 7.36 | 8.14±0.23 | 25.68 | 25.35 | Irregulars |
| 18444 | 3.92±1.97 | - | 26.11 | 10.05±0.17 | 9.11 | 13.25±0.13 | 26.98 | 26.46 | Irregulars |
| 18482 | 0.87±0.44 | - | 28.16 | 8.51±0.15 | 4.91 | 10.10±0.09 | 28.02 | 27.54 | Irregulars |
| 18684 | 1.26±0.64 | - | 26.88 | 9.03±0.08 | 4.45 | 10.66±0.07 | 26.91 | 26.68 | Uncertain |
| 19214 | 0.89±0.45 | - | 23.40 | 9.41±0.05 | 11.66 | 10.11±0.10 | 25.37 | 24.42 | Irregulars |
| 19256 | 0.38±0.20 | - | 25.54 | 7.98±0.18 | 6.15 | 9.42±0.28 | 27.50 | 27.13 | Irregulars |
| 20380 | 0.70±0.36 | - | 24.37 | 8.71±0.09 | 9.34 | 9.98±0.09 | 25.45 | 25.40 | Irregulars |
| 20901 | 0.60±0.31 | 0.6190±0.0001 | 21.57 | 10.24±0.05 | 15.28 | 10.75±0.05 | 23.78 | 23.01 | Spirals+HII regions |
| 21046 | 0.54±0.28 | 0.6207±0.1552 | 23.00 | 9.20±0.04 | 23.88 | 10.00±0.05 | 25.28 | 24.17 | Disk galaxies |
| 21360 | 0.63±0.32 | - | 25.17 | 8.20±0.03 | 7.30 | 10.09±0.10 | 26.28 | 25.96 | Irregulars |
| 22420 | 0.58±0.30 | 0.6150±0.0001 | 21.38 | 10.51±0.03 | 14.02 | 11.18±0.02 | 23.85 | 23.15 | Spirals+HII regions |
| 22556 | 0.59±0.30 | 0.6094±0.1524 | 23.04 | 9.51±0.03 | 17.88 | 10.07±0.31 | 24.38 | 24.03 | Disk galaxies |

*-Continuation*

| CANDELS ID | photo-z | spec-z | $m_R$ | Mass | Diameter | LIR | FUV | NUV | Morph |
|---|---|---|---|---|---|---|---|---|---|
| (1) | (2) | (3) | (4) | (5) | (6) | (7) | (8) | (9) | (10) |
| 22962 | 0.55±0.28 | - | 25.42 | 8.15±0.16 | 8.21 | 9.96±0.12 | 26.14 | 26.15 | BCD |
| 23065 | 0.68±0.35 | - | 26.54 | 7.88±0.23 | 4.20 | 10.56±0.03 | 26.96 | 26.63 | BCD |
| 23137 | 0.57±0.29 | 0.6045±0.0001 | 22.83 | 8.97±0.16 | 14.28 | 10.55±0.08 | 23.19 | 23.24 | Irregulars |
| 23248 | 0.61±0.31 | 0.6194±0.0001 | 21.51 | 10.17±0.05 | 9.83 | 10.91±0.07 | 23.04 | 22.59 | Spirals+HII regions |
| 24623 | 0.60±0.31 | 0.6162±0.3081 | 25.06 | 8.47±0.42 | 4.22 | 10.09±0.29 | 25.71 | 25.78 | BCD |
| 26132 | 0.60±0.31 | 0.6200±0.0001 | 24.19 | 9.03±0.13 | 8.25 | 11.76±0.13 | 25.91 | 25.02 | Disk galaxies |
| 26460 | 0.71±0.36 | - | 26.01 | 7.81±0.13 | 3.37 | 10.66±0.06 | 26.56 | 26.61 | BCD |
| 31370 | 0.51±0.26 | - | 27.76 | 7.46±0.21 | 12.00 | 10.93±0.06 | 28.08 | 27.83 | Uncertain |
| 34118 | 1.35±0.68 | - | 27.61 | 8.47±0.13 | 3.60 | 11.32±0.48 | 27.44 | 27.50 | Uncertain |

Table 9: Calculations performed over the sample. The columns show the values: (1) CANDELS ID. (2) Luminosity distance (Mpc). (3) Observed $H\alpha$ luminosity ( $10^{40}$erg s$^{-1}$). (4) Extinction corrected $H\alpha$ luminosity ( $10^{40}$erg s$^{-1}$). (5) Observed star formation rate ( $M_\odot\,yr^{-1}$). (6) Extinction corrected star formation rate ( $M_\odot\,yr^{-1}$). (7) $H\alpha$ extinction (mag). (8) Observed equivalent width ( Å). (9) Rest-frame equivalent width ( Å).

| CANDELS ID | $d_l$ | $L_{obs}$ | $L_{cor}$ | $SFR_{obs}$ | $SFR_{cor}$ | $A_{H\alpha}$ | $EW_{obs}$ | $EW_{rf}$ |
|---|---|---|---|---|---|---|---|---|
| (1) | (2) | (3) | (4) | (5) | (6) | (7) | (8) | (9) |
| 11513 | 3602 | 0.37±0.26 | 0.79±0.59 | 0.03±0.02 | 0.06±0.05 | 0.83±0.22 | 115.4±136.7 | 71.7±84.9 |
| 12039 | 3602 | 0.42±0.08 | 0.50±0.18 | 0.03±0.01 | 0.04±0.01 | 0.20±0.31 | 1038.9±290.6 | 645.3±180.5 |
| 13781 | 3666 | 5.54±0.32 | 6.29±0.53 | 0.44±0.03 | 0.50±0.04 | 0.14±0.07 | 63.7±4.6 | 39.3±2.8 |
| 14122 | 3602 | 0.51±0.25 | 1.70±0.84 | 0.04±0.02 | 0.13±0.07 | 1.30±0.07 | 223.2±301.4 | 138.6±187.2 |
| 15282 | 3674 | 8.80±0.36 | 8.37±0.37 | 0.70±0.03 | 0.66±0.03 | 0 | 76.2±4.1 | 47.0±2.6 |
| 15286 | 3602 | 0.54±0.34 | 0.78±0.49 | 0.04±0.03 | 0.06±0.04 | 0.40±0.06 | 38.5±26.3 | 23.9±16.6 |
| 15398 | 3666 | 6.97±0.39 | 11.22±0.85 | 0.55±0.03 | 0.89±0.07 | 0.52±0.06 | 36.2±2.2 | 22.3±1.3 |
| 15650 | 3602 | 2.02±0.36 | 10.76±2.54 | 0.16±0.03 | 0.85±0.20 | 1.82±0.17 | 239.4±126.9 | 148.7±78.8 |
| 15784 | 3602 | 0.45±0.32 | 1.87±1.35 | 0.04±0.03 | 0.15±0.11 | 1.54±0.09 | 33.1±25.3 | 20.5±15.7 |
| 16155 | 3602 | 0.33±0.30 | 1.98±1.78 | 0.03±0.02 | 0.16±0.14 | 1.95±0.07 | 65.4±73.2 | 40.6±45.5 |
| 16644 | 3602 | 0.34±0.40 | 0.85±1.00 | 0.03±0.03 | 0.07±0.08 | 0.99±0.07 | 8.4±10.0 | 5.2±6.2 |
| 16798 | 3602 | 1.45±0.29 | 4.45±0.92 | 0.11±0.02 | 0.35±0.07 | 1.22±0.07 | 363.0±310.0 | 225.5±192.6 |
| 16839 | 3602 | 0.30±0.32 | 0.42±0.46 | 0.02±0.03 | 0.03±0.04 | 0.39±0.13 | 14.3±15.6 | 8.9±9.7 |
| 16845 | 3602 | 0.71±0.34 | 1.29±0.62 | 0.06±0.03 | 0.10±0.05 | 0.65±0.08 | 66.5±40.7 | 41.3±25.3 |
| 17058 | 3687 | 5.65±0.43 | 6.91±0.56 | 0.45±0.03 | 0.55±0.04 | 0.22±0.03 | 18.6±1.4 | 11.5±0.9 |
| 17075 | 3602 | 0.75± 0.29 | 4.23± 1.68 | 0.06±0.02 | 0.33±0.13 | 1.88±0.13 | 170.4±144.4 | 105.8±89.7 |
| 17183 | 3602 | 1.86±0.38 | 3.34±0.71 | 0.15±0.03 | 0.26±0.06 | 0.64±0.07 | 181.3±89.0 | 112.6±55.3 |
| 17393 | 3602 | 1.19±0.31 | 1.92±0.52 | 0.09±0.02 | 0.15±0.04 | 0.52±0.06 | 62.5±20.0 | 38.8±12.4 |
| 17503 | 3602 | 0.31±0.21 | 0.83±0.57 | 0.02±0.02 | 0.07±0.05 | 1.06±0.14 | 195.1±315.6 | 121.2±196.0 |
| 17686 | 3602 | 0.58±0.15 | 2.03±0.54 | 0.05±0.01 | 0.16±0.04 | 1.35±0.07 | 5316.8±73237.4 | 3302.3±45489.1 |
| 17704 | 3602 | 0.30±0.31 | 0.27±0.27 | 0.02±0.02 | 0.02±0.02 | 0 | 3.8 ± 51.2±60.0 | 31.8±37.3 |
| 18444 | 3602 | 0.27±0.29 | 3.87±4.26 | 0.02±0.02 | 0.31±0.34 | 2.90±0.12 | 41.3±50.2 | 25.7±31.2 |
| 18482 | 3602 | 0.49±0.25 | 1.06±0.55 | 0.04±0.02 | 0.08±0.04 | 0.85±0.08 | 150.5±155.6 | 93.5±96.6 |
| 18684 | 3602 | 0.26±0.27 | 0.61±0.62 | 0.02±0.02 | 0.05±0.05 | 0.92±0.07 | 64.5±82.4 | 40.0±51.2 |
| 19214 | 3602 | 0.49±0.38 | 0.63±0.48 | 0.04±0.03 | 0.05±0.04 | 0.27±0.06 | 6.9±5.3 | 4.3±3.3 |
| 19256 | 3602 | 0.31±0.33 | 0.44±0.45 | 0.02±0.03 | 0.03±0.04 | 0.35±0.14 | 40.9±46.7 | 25.4±29.0 |
| 20380 | 3602 | 1.23±0.32 | 1.51±0.41 | 0.10±0.03 | 0.12±0.03 | 0.23±0.05 | 44.9±13.3 | 27.9±8.2 |
| 20901 | 3666 | 7.44±0.46 | 9.52±0.69 | 0.59±0.04 | 0.75±0.05 | 0.27±0.04 | 23.3±1.5 | 14.4±0.9 |
| 21046 | 3679 | 4.63±0.37 | 5.58±0.49 | 0.37±0.03 | 0.44±0.04 | 0.20±0.04 | 59.4±5.8 | 36.6±3.6 |
| 21360 | 3602 | 0.40±0.36 | 0.60±0.54 | 0.03±0.03 | 0.05±0.04 | 0.44±0.07 | 27.1±25.3 | 16.8±15.7 |
| 22420 | 3638 | 20.46± 0.38 | 32.25±1.45 | 1.62±0.03 | 2.55±0.11 | 0.49±0.04 | 34.5±0.7 | 21.4±0.4 |
| 22556 | 3597 | 0.83± 0.35 | 0.91±0.39 | 0.07±0.03 | 0.07±0.03 | 0.10±0.11 | 12.6±5.4 | 7.8±3.3 |
| 22962 | 3602 | 1.12± 0.35 | 1.53±0.49 | 0.09±0.03 | 0.12±0.04 | 0.35±0.07 | 144.3±90.1 | 89.6±56.0 |

*-Continuation*

| CANDELS ID | $d_l$ | $L_obs$ | $L_cor$ | $SFR_{obs}$ | $SFR_{cor}$ | $A_{H\alpha}$ | $EW_{obs}$ | $EW_{rf}$ |
|---|---|---|---|---|---|---|---|---|
| (1) | (2) | (3) | (4) | (5) | (6) | (7) | (8) | (9) |
| 23065 | 3602 | 0.68± 0.13 | 1.51±0.31 | 0.05±0.01 | 0.12±0.02 | 0.87±0.05 | 1038.9±289.5 | 645.3±179.8 |
| 23137 | 3562 | 0.50± 0.44 | 0.55±0.48 | 0.04±0.03 | 0.04±0.04 | 0.10±0.04 | 6.5±5.7 | 4.0±3.5 |
| 23248 | 3669 | 30.58± 0.47 | 37.09±1.62 | 2.42±0.04 | 2.93±0.13 | 0.21±0.04 | 77.9±1.6 | 48.1±1.0 |
| 24623 | 3646 | 2.19± 0.34 | 2.95±0.60 | 0.17±0.03 | 0.23±0.05 | 0.32±0.14 | 104.8±25.4 | 64.8±15.7 |
| 26132 | 3674 | 0.97± 0.37 | 3.51±1.39 | 0.08±0.03 | 0.28±0.11 | 1.39±0.11 | 22.0±8.7 | 13.6±5.4 |
| 26460 | 3602 | 0.60± 0.36 | 1.29±0.78 | 0.05±0.03 | 0.10±0.06 | 0.83±0.06 | 92.0±81.5 | 57.2±50.6 |
| 31370 | 3602 | 0.29±0.25 | 1.07±0.92 | 0.02±0.02 | 0.08±0.07 | 1.44±0.07 | 100.4±131.7 | 62.4±81.8 |
| 34118 | 3602 | 0.51± 0.24 | 2.08±1.21 | 0.04±0.02 | 0.16±0.10 | 1.53±0.36 | 252.1±369.1 | 156.6±229.2 |

## B. RGB images

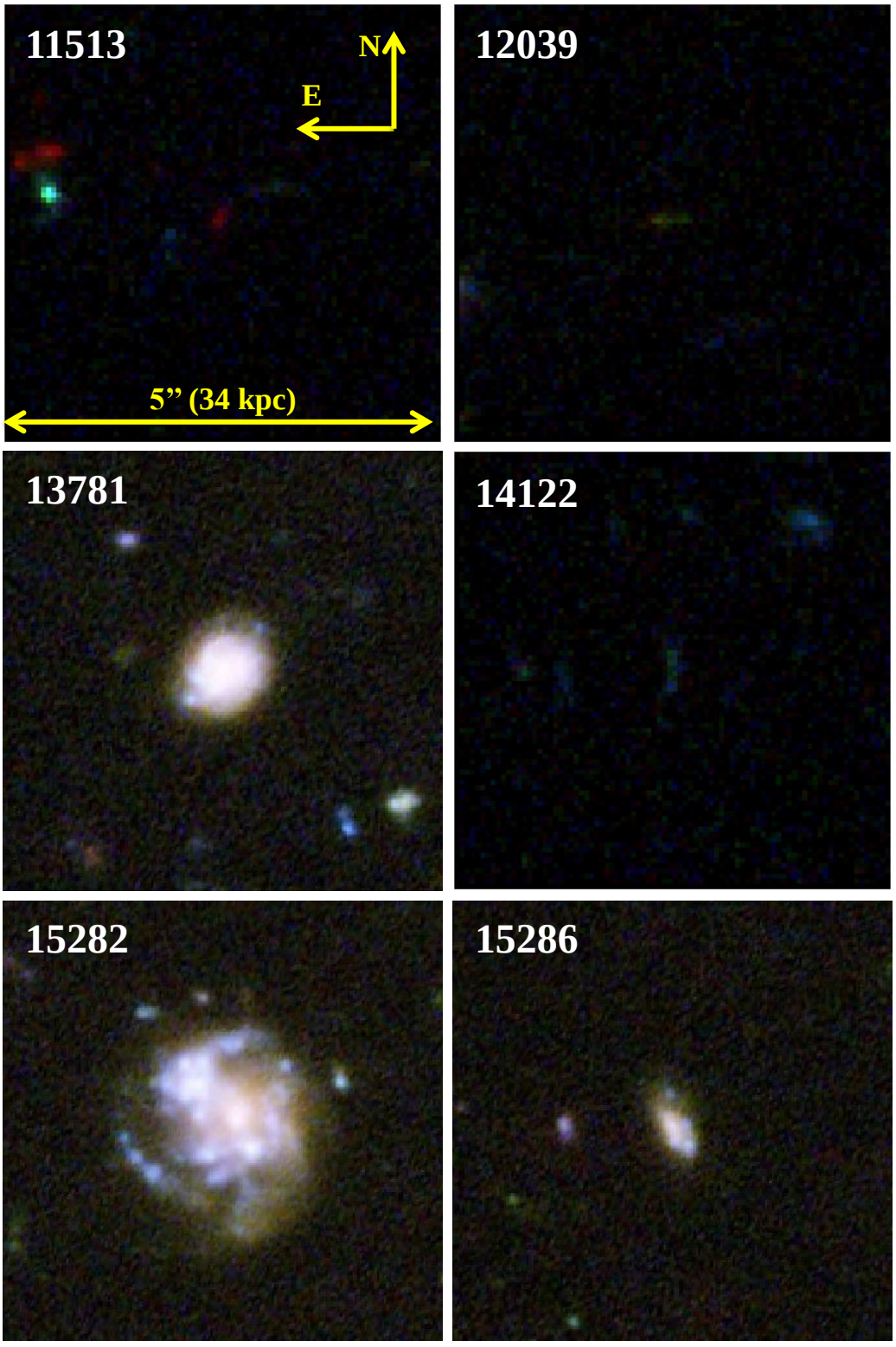

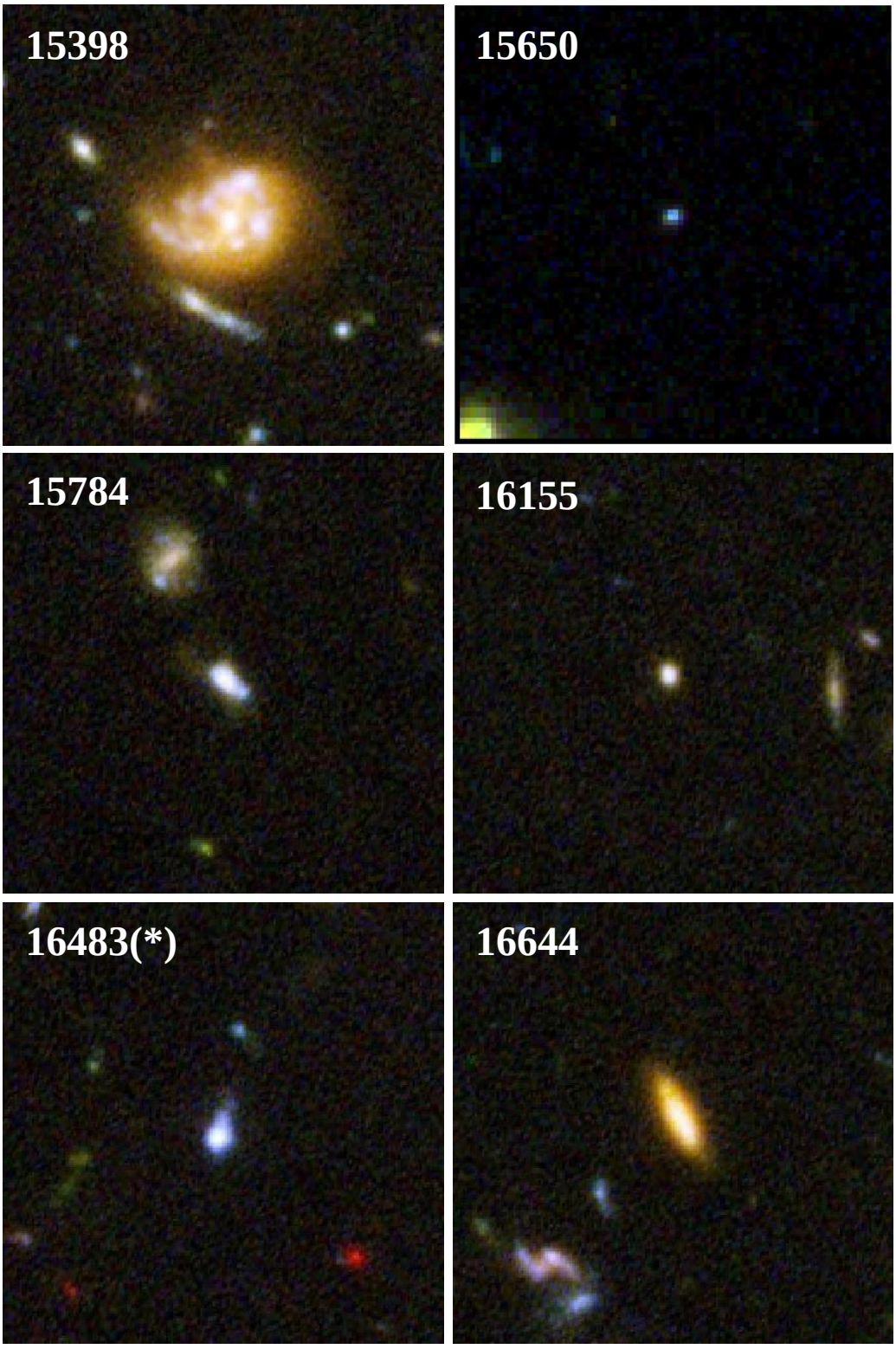


(*) 16483 correspond to an object with spec-z=1.1730

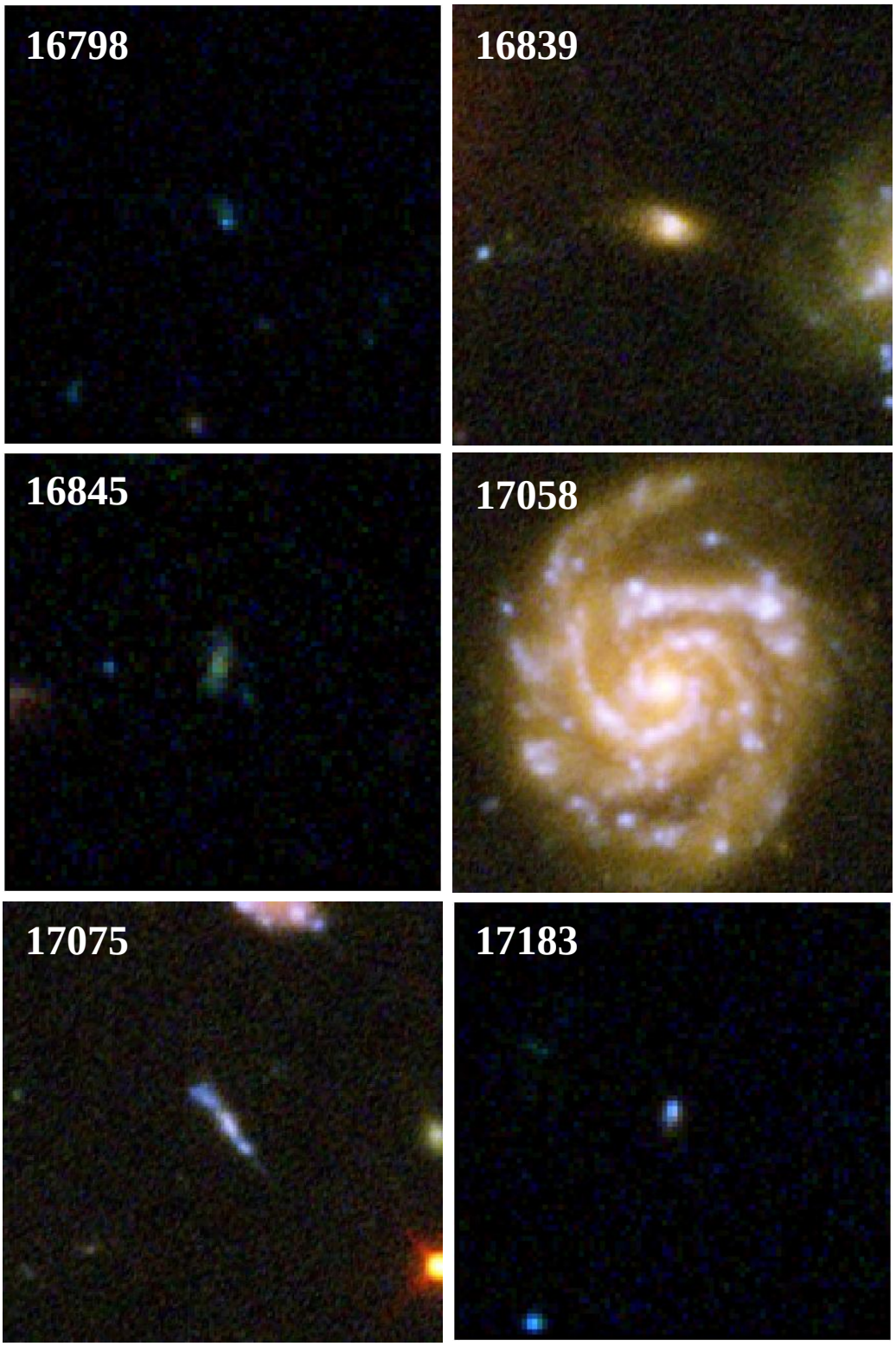
16798
16839
16845
17058
17075
17183

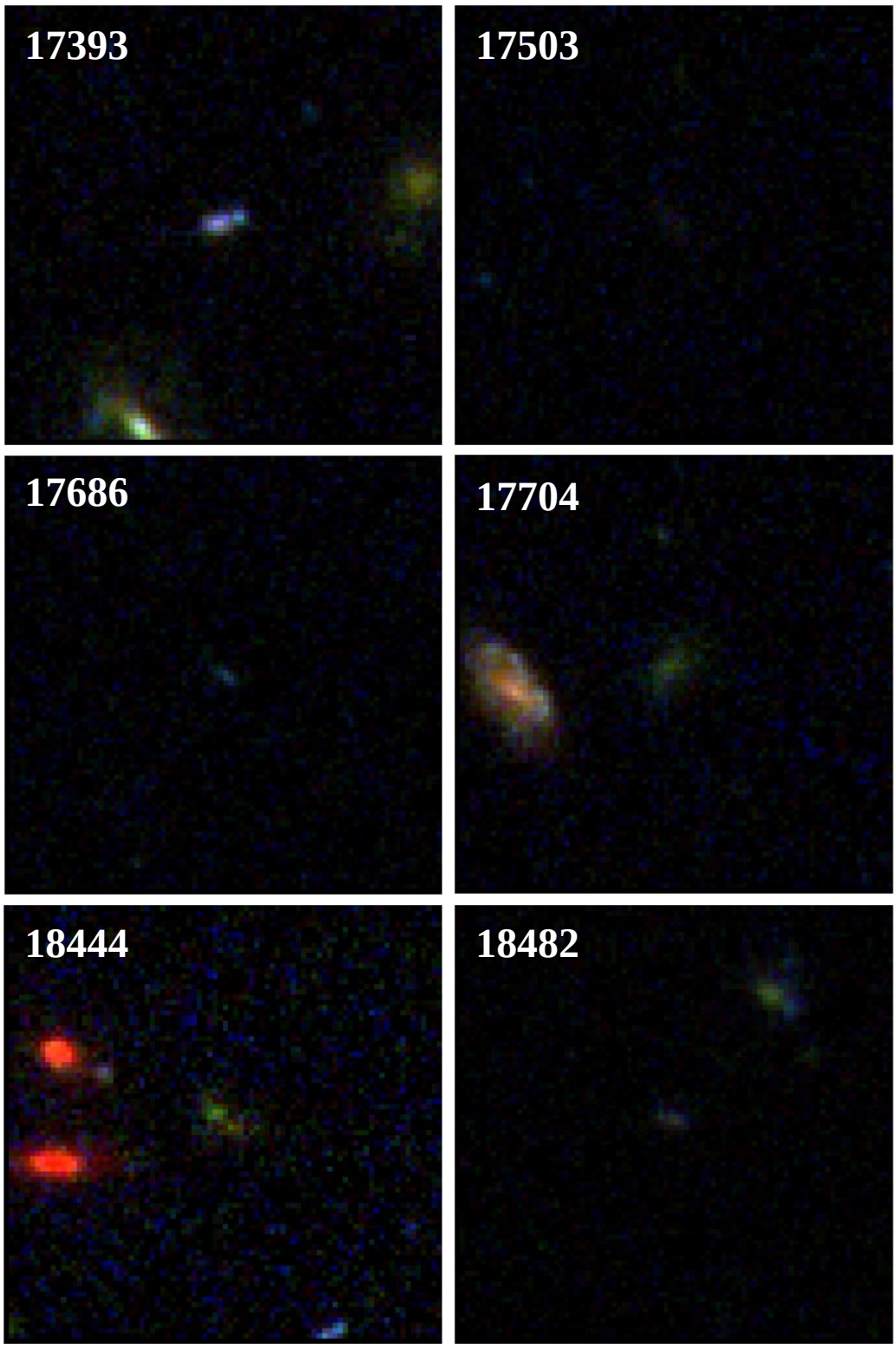
17393
17503
17686
17704
18444
18482

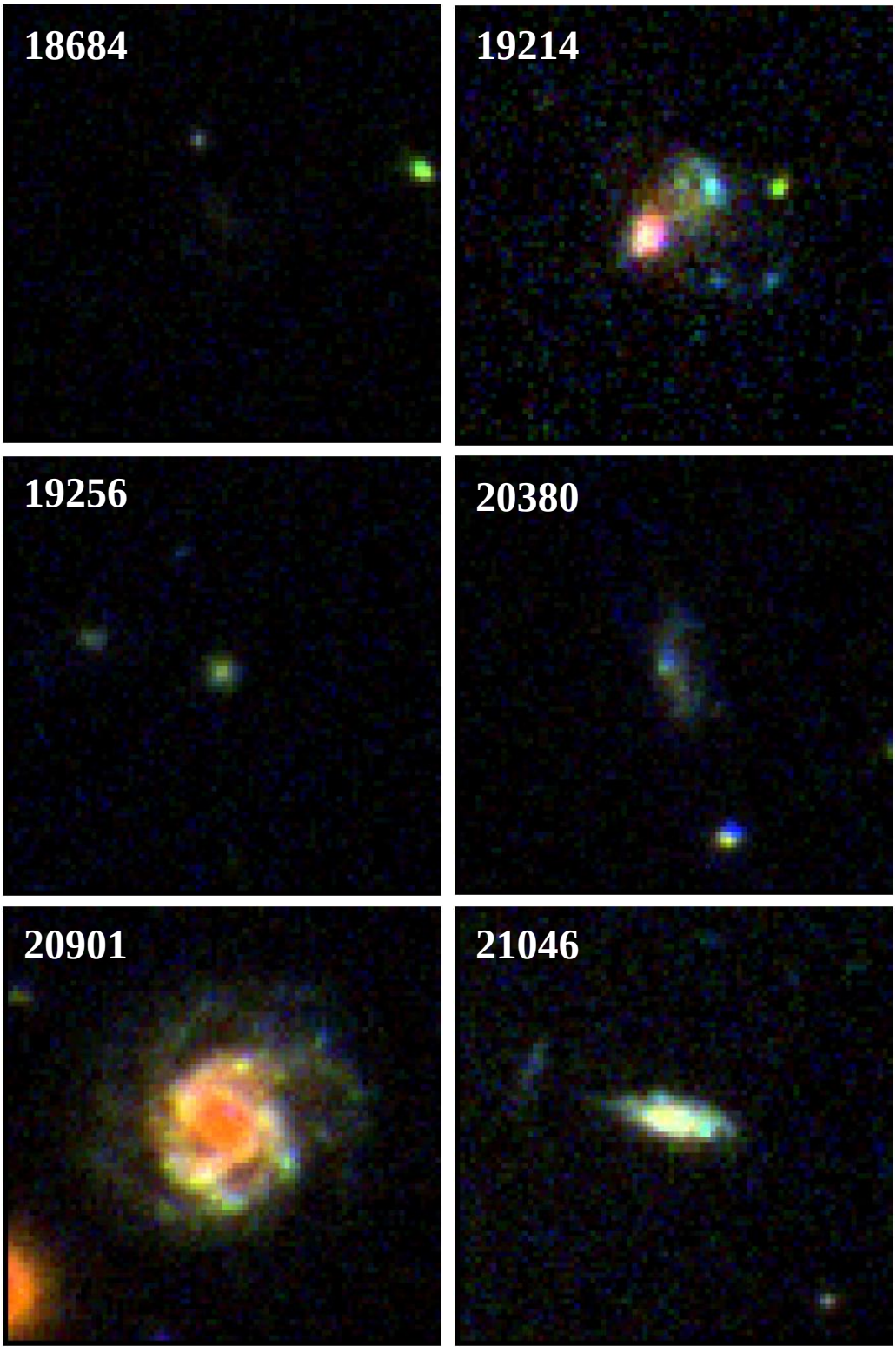
18684
19214
19256
20380
20901
21046

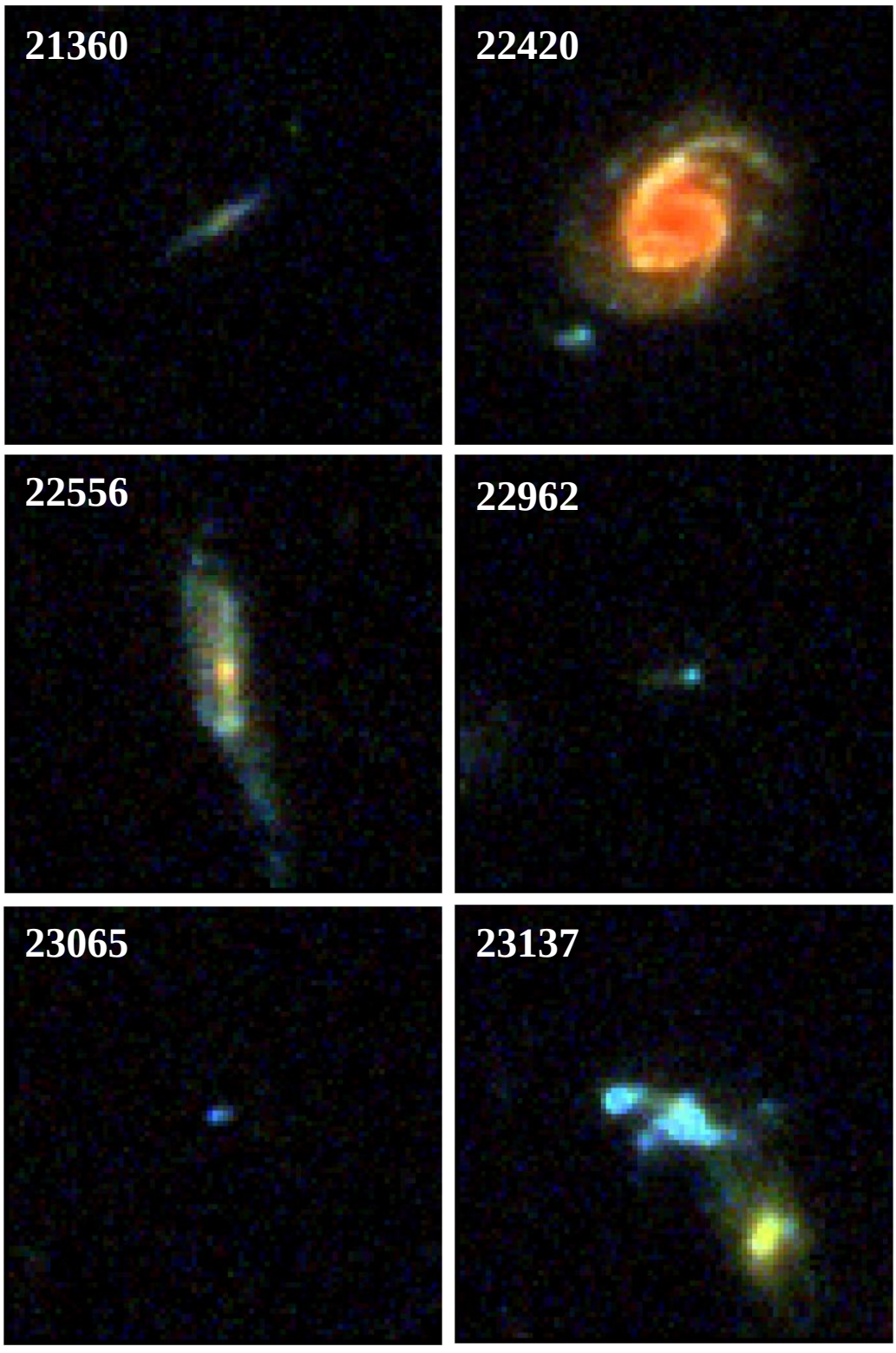
21360
22420
22556
22962
23065
23137

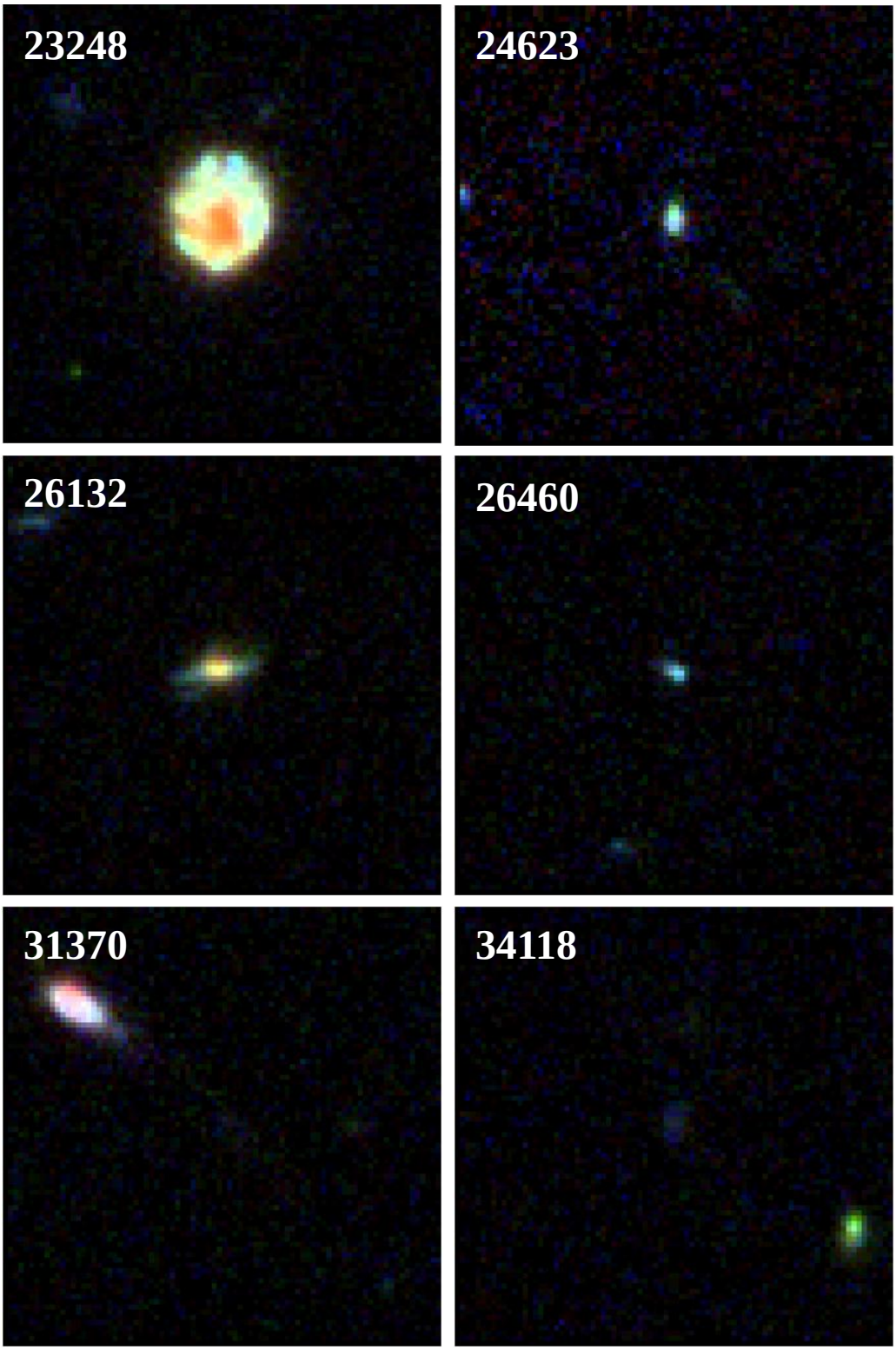
23248
24623
26132
26460
31370
34118

# C. Spectra

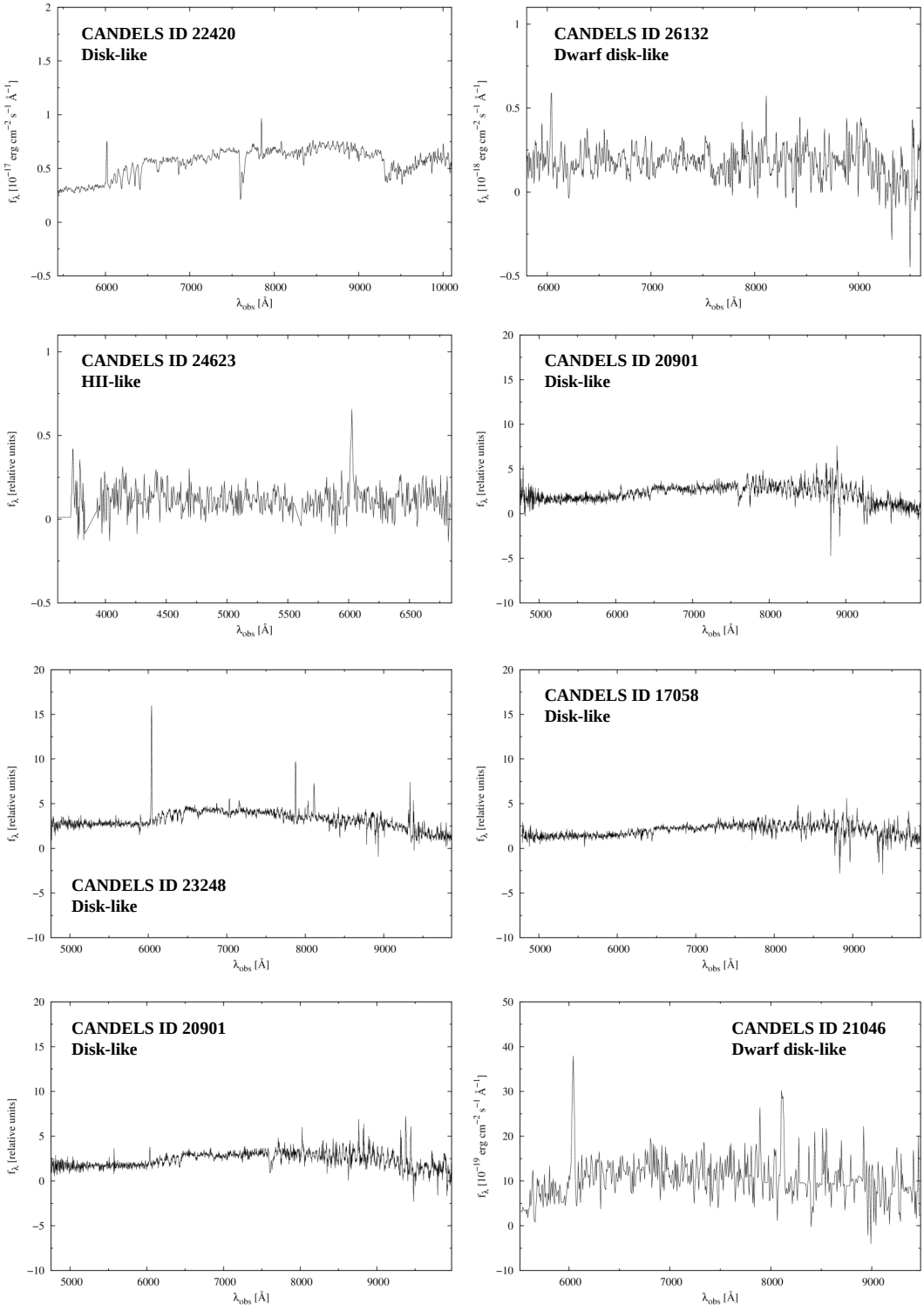
CANDELS ID 22420
Disk-like
CANDELS ID 26132
Dwarf disk-like
CANDELS ID 24623
HII-like
CANDELS ID 20901
Disk-like
CANDELS ID 23248
Disk-like
CANDELS ID 17058
Disk-like
CANDELS ID 20901
Disk-like
CANDELS ID 21046
Dwarf disk-like
λobs [Å]
fλ [relative units]